

**SAHRAEI FAILURE CRITERIA FOR DETECTION OF SHORT
CIRCUIT IN LITHIUM-ION BATTERIES**

A Dissertation
Submitted to
the Temple University Graduate Board

In Partial Fulfillment
of the Requirements for the Degree
DOCTOR OF PHILOSOPHY

by
Yihan Song
December 2025

Examining Committee Members:

Elham Sahraei, Advisory Chair, Mechanical Engineering
Fei Ren, Mechanical Engineering
Kurosh Darvish, Mechanical Engineering
Marian Bulla, Altair Engineering, Inc.
Shaopin Song, External Reader, Tesla Motors

©
Copyright
2025

by

YIHAN SONG
All Rights Reserved

ABSTRACT

The increasing reliance on Li-ion batteries for Electric Vehicle (EV) propulsion brings forth significant safety challenges, particularly in ensuring battery resilience under mechanical abuse and accidental impacts. A critical concern is the potential for internal fracture within battery cells, which can trigger short circuits, leading to thermal runaway and explosions. Consequently, understanding battery behavior under various loading conditions and developing predictive models for failure is essential for enhancing safety and optimizing protective structures in EVs. This dissertation presents a comprehensive analysis of Li-ion battery behavior under multiple loading scenarios, supported by two novel modeling approaches: a universal homogenized model for cylindrical cells and the Sahraei Failure Criterion for short circuit prediction.

The first part of this research focuses on the development of a universal homogenized model for 18650 cylindrical battery cells, capable of accurately predicting cell behavior under axial, lateral, and three-point bending loads. Unlike previous models that addressed one or two loading conditions, this model incorporates uncoupled axial and lateral property calibrations and employs anisotropic crushable foam modeling for enhanced accuracy. The model is validated through experimental data and demonstrates superior performance in predicting cell response, particularly in axial and bending scenarios.

The second part introduces the Sahraei Failure Criterion, a universal failure model designed to predict internal fractures and short circuits in both cylindrical and pouch cells. This criterion, derived from microstructural simulations of the electrode-separator assembly, is implemented in commercial simulation software, including Altair RADIOSS and Ansys LS-DYNA. The failure model is validated under various loading conditions,

such as hemispherical and rod indentations, in-plane loading, and three-point bending. By defining the jellyroll's failure strain based on the interaction of compressive and tensile strains, the model accurately predicts the onset of internal fractures, providing a critical tool for battery safety analysis. Furthermore, real physics has been added to the base failure criteria. By testing battery cell's mechanical response under different physical conditions, enhanced failure criteria have been built and validated.

Together, these models offer a robust framework for understanding and predicting Li-ion battery behavior under mechanical stress, contributing to safer EV designs and more effective protective structures. This research advances the field by combining detailed material calibrations and computational modeling, offering a comprehensive solution to address the safety concerns associated with Li-ion batteries in electric vehicles.

ACKNOWLEDGMENTS

It is with profound gratitude that I acknowledge my supervisor, Dr. Elham Sahraei. Dr. Sahraei's unwavering support and guidance have been instrumental not only in my academic journey but also profoundly impactful on my personal development.

Her deep expertise and scholarly insight were invaluable, constantly challenging me to strive for excellence. She truly led by example, demonstrating the qualities of a dedicated researcher and an exemplary role model. Beyond academia, Dr. Sahraei generously provided essential guidance on navigating life's challenges and professional interactions, offering wisdom that I will carry forward long after my studies conclude.

I would also like to extend my sincere gratitude to Dr. Fei Ren and Dr. Kurosh Darvish for their invaluable assistance during critical milestones of my doctoral journey. Their expertise and unwavering support were essential to my success in both the preliminary examination and the final dissertation defense. I am deeply thankful for the time they invested, their insightful feedback, and the encouragement they provided throughout the process.

I would like to extend my heartfelt thanks to Dr. Shaopin Song, who served as my mentor during my internship at Tesla. His guidance was invaluable in helping me navigate complex technical challenges and deepen my understanding of real-world engineering applications. Beyond his exceptional expertise and leadership, Dr. Song demonstrated a genuine commitment to my professional growth, offering insightful advice and steadfast support at every stage. His mentorship not only enhanced my technical skills but also inspired me to pursue excellence with integrity and innovation. I am deeply grateful for the opportunity to have learned from such an accomplished and generous individual.

I would like to express my deepest gratitude to Marian Bulla for his generous support and invaluable contributions throughout my PhD studies. During the four years of collaboration, he not only provided professional guidance and patient assistance in the programming and development in OpenRadioss/Radioss but also offered insightful suggestions in tackling technical challenges and improving model validation implementations. Through our close collaboration, we successfully accomplished the development and implementation of the SAHRAEI Failure Model and the User-Defined Honeycomb Model. These achievements laid a solid technical foundation for my research and significantly broadened my knowledge and skills in numerical simulation and model development. I am sincerely grateful for his continuous support, patience, and encouragement during my doctoral journey.

I would like to acknowledge the funding from multiple sources for this research. This includes support from Temple University Startup funds, MIT Industrial battery consortium, and Office of Naval Research Contracts N000141912351 and N000142312612. This research includes calculations carried out on HPC resources supported in part by the National Science Foundation through major research instrumentation grant number 1625061 and by the US Army Research Laboratory under contract number W911NF-16-2-0189. I also like to express thanks to the OpenRadioss team for supporting the implementation of the code and resolving all technical questions throughout the project.

This dissertation includes material for which public release has been approved by the Office of Naval Research. Public Release Approval DCN# 2025-10-1-1538, dated 10/23/2025.

TABLE OF CONTENTS

	Page
ABSTRACT.....	iii
ACKNOWLEDGMENTS	v
LIST OF TABLES	x
LIST OF FIGURES	xi
CHAPTER	
1. INTRODUCTION	1
1.1 Background.....	1
1.2 Review of the previous models for Li-ion battery cells and failure models.....	2
1.1.1 Cylindrical & Pouch cell models	2
1.1.2 Failure models.....	3
1.3 Failure model development.....	5
1.4 Effects of temperature, SoC, strain rate and aging	6
1.4.1 Effects of temperature.....	6
1.4.2 Effects of SoC	9
1.4.3 Effects of strain rate.....	9
1.4.1 Effects of aging	10
2. METHODS	12
2.1 Introduction.....	12
2.2 Battery Specification.....	12
2.3 Experiments	13
2.3.1 Flat Compression	15

2.3.2 Rod indentation.....	15
2.3.3 Hemispherical indentation.....	15
2.3.4 Three-point bending.....	16
2.3.5 Axial/In-plane compression.....	16
2.4 RVE based Sahraei failure model.....	17
3. COMPUTATIONAL MODELING.....	23
3.1 Introduction.....	23
3.2 18650 cylindrical cell model.....	23
3.2.1 Shell casing material.....	23
3.2.2 Shell casing failure model.....	24
3.2.3 Jellyroll material.....	25
3.2.4 Finite element modeling of Shell Casing and jellyroll.....	30
3.3 Pouch cell model.....	32
3.3.1 Jellyroll material model.....	32
3.4 Sahraei failure model.....	34
3.5 Element orientation.....	35
4. VALIDATION OF THE STRUCTURAL ONLY MODEL.....	38
4.1 Introduction.....	38
4.2 Comparison between simulation and experiment.....	38
4.3 Discussion.....	44
4.3.1 Comparison of the failure criteria and anisotropy of casing material.....	44
4.3.2 Comparison of the anisotropy of jellyroll material.....	45
4.3.3 Comparison of failure curve.....	48

5. ENHANCEMENT OF SAHRAEI FAILURE CRITERIA WITH REAL PHYSIC EFFECTS	50
5.1 Introduction.....	50
5.2 Method	51
5.2.1 Battery specification	51
5.2.2 Test method.....	51
5.3 Finite element modeling	56
5.3.1 Material modeling.....	56
5.3.2 Failure criteria enhancement.....	57
5.4 Model validation	59
5.4.1 Failure validation of rod test under different temperature	59
5.4.2 Failure validation of rod test under different SoC	60
5.4.3 Failure validation of rod test under different strain rate	62
5.4.4 Model capability for aged cell prediction	62
6. CONCLUSION	65
7. CONTRIBUTIONS	67
REFERENCES	68
APPENDIX.....	77

LIST OF TABLES

Table	Page
1. Contribution comparison with previous works.....	8
2. Parameters for combined Voce-Swift law and the fracture locus.....	24
3. Material properties for cylindrical (cell A and B) cell's jellyroll	32
4. Material properties for pouch cell's jellyroll	33
5. R square for all simulations	44
6. Nomenclature in the equation	58
7. Aging effect comparison with literature	63

LIST OF FIGURES

Figure	Page
1. Experiment schematics and results	14
2. Sahraei 2016 model failure strain versus ratio of compressive to tensile strain	20
3. Sequence of different loading and failure of the RVE.....	22
4. Axial compression of the cylindrical cell	29
5. FEM model and material inputs for isotropic/anisotropic of the jellyroll	31
6. Finite element model of the jellyroll with element orientation.....	37
7. Simulation results of cell A.....	41
8. Simulation results of cell B.....	42
9. Simulation results of pouch cell.....	43
10. Comparison between different failure criteria	45
11. Comparison between anisotropic and isotropic material for axial compression	46
12. Failure curve comparison for cell A, cell B and pouch cell.....	49
13. Rod indentation at different temperatures.....	52
14. Rod indentation under different SoC	53
15. Dynamic rod impact test	55
16. Model validation for different temperature rod indentation test.....	60
17. Model validation for different SoC rod indentation test.....	61
18. Comparison between dynamic and static rod test.....	62

CHAPTER 1

INTRODUCTION

1.1 Background

Electric vehicles (EVs) make it possible to use clean energy resources for transportation. This is one of the most promising ways to respond to the world's energy challenge. As a major energy storage unit, batteries play an important role in many industries, including vehicle manufacturing¹⁻⁵. Among all options, Li-ion batteries currently show the best prospects for EV applications. They have high specific capacity, high efficiency in charging and discharging, long cycle life and an acceptable cost⁶. As typical form factors for Li-ion battery cells, 18650 cylindrical battery cells and pouch/prismatic cells have geometry and electrical capabilities that make them one of the most common cells used for EVs⁷. However, it should be noted that Li-ion batteries are sensitive to impact and crushing, which means ensuring their safety is a major challenge for the EV industry. Manufacturers designing EVs must consider the potential abuse conditions on batteries from various sources, such as overcharging/discharging, impact, crush, and mechanical vibration⁸. An impact on the battery can cause deformation and failure of interior components such as electrodes and separators and can possibly lead to an internal short circuit inside a battery cell. Depending on the chemistry of the cell, an internal short circuit may generate huge amounts of heat and increase the pressure inside the cell, leading to a violent thermal runaway in extreme cases. For a single battery cell, this procedure is irreversible and can easily spread to adjacent cells causing fire and explosion in a battery pack and the whole EV⁹⁻¹¹. Therefore, the safety design of Li-ion batteries is a key factor. To get a better understanding about the limitations of the battery under different loading cases, many

experiments have been designed to quantify battery behavior under mechanical abuse^{12,13}. Furthermore, those test results have been used to generate Finite Element Models (FEM) which can simulate a car crash or accident during the design cycle of an EV. Such models are an essential tool to reduce the costs of vehicle design by reducing the number of required tests. Additionally, they provide a tool to improve understanding of the ongoing processes within a Li-ion cell during mechanical loads. This highlights the need for having a proper model to get accurate prediction on deformation and internal failure of the battery.

1.2 Review of the previous models for Li-ion battery cells and failure models

1.1.1 Cylindrical & Pouch cell models

Battery manufacturers usually do not provide any information on the mechanical properties of cell components. Therefore, researchers have addressed the needs for testing and modeling mechanical properties of the batteries. In 2012, the first set of mechanical tests on full cylindrical and pouch lithium-ion cells with first homogenized models to predict their deformation and failure were published by Sahraei et al^{14,15}. Over the past ten years, several other models had been proposed with different materials¹⁶ and failure models for the jellyroll/electrode stack and shell casing of the cell^{17,18,27,19-26}. Additionally, there had been studies focused on testing and modeling deformation and failure of single components of a battery cell like electrodes and separators²⁸⁻³⁰. Other researchers had extended components and cell level models into evaluation of the response at the battery pack level^{28,31,32}. Relation between failure strain and state of charge had been discussed by Xu et al, 2016³³. The most insight into the fracture mechanism of the jellyroll/electrode

stack comes from studies of deformation at the micro structural level, which is the basis of the research presented in this work^{28,34-38}.

1.1.2 Failure models

Here, we will first review the most common failure models discussed and used in the literature in general and then focus on the ones that have been applied to the jellyroll/electrode stack of lithium-ion batteries. One typical type of failure model is the simple single parameter one, where defining a single indicator for failure, like strain value or stresses value is identified as the criterion. For body-centered cubic (BCC) materials, maximum principle stress is commonly used as indicator of the brittle fracture predictions^{39,40}. Maximum shear stress is one of the oldest failure criteria used for rock or soil⁴¹. Maximum principal strain failure model has also been very popular for battery simulations. From the first use by Sahraei et al⁴², lots of studies had been using the principle strain as the failure indicator^{14,21,43}. For this model, the failure strain is calibrated from through-thickness loading experiments. This model then predicts failure accurately for dominantly through-thickness compressive loads, such as local indentations with a hemispherical/flat punch or rod indentation. The problem with this single parameter failure model is that it cannot have a good prediction in cases with major tensile loading or when loads are not in through-thickness direction, such as three-point bending and in-plane loading. Another very common type of failure model is the universal failure model. This model usually defines failure strain or stress as a function. Typical examples are Johnson-Cook (JC), Cockcroft-Latham (CL) and modified Mohr-Coulomb (MMC) models. These models define failure strain as a function of triaxiality or both triaxiality and lode angle parameter. It has been proved that failure strain for metals behave differently under

compression and tension. For battery models, failure of shell casing, as the major load bearing metal component of the cylindrical and prismatic cells, had been predicted accurately with such models^{43,44}, where the cell has been modeled with two major components, a homogenized jellyroll and a metal casing. Wang et al 2019 also used this method to account for the failure of shell casing in their detailed models⁴⁵. Those failure criteria can also be used for the jellyroll metal components, such as metal current collectors^{43,46-48}. However, this kind of criteria has not been reported to be successful in prediction of failure for a homogenized model of the jellyroll/electrode stack. Since the electrode stack/ jellyroll is comprised of several layers of porous polymeric/granular materials in addition to the metallic ones, a universal failure model, considering the complexities of all layers and the interactions between them in various types of loadings, must be identified to make accurate predictions for a homogenized material representing all layers.

Table 1 shows the previous battery cell models with failure criteria coupled. Many previous works predicted the jellyroll failure with single parameter criteria. The most popular one is maximum principal failure strain criterion. For this model, a single failure strain value is calibrated, usually from simulation of a hemispherical punch loading case, using the location of force drop, which coincides with location of voltage drop for the cases with voltage measurements, as the exact position of element erosion. This failure model has been validated with a few loading cases including the ones with major through-thickness compression loading. However, when the loading becomes more complex, the failure will not be predicted correctly with this failure model. In some past studies, to track the changes in failure strain for different load cases, the failure strain was recalibrated.

However, this cannot be considered a universal failure model when a new calibration is needed for a new load case. The past work of some of the current authors mostly fall under this category^{25,43,47,48}. In an attempt to find alternative failure models, Chung et al proposed using stress-based Mohr Columb criteria and validated that again for dominantly through-thickness compression cases of hemispherical and punch indentations²⁷. Greve et al and Zhang & Xu et al proposed their own failure criteria based on modeling various loading cases and monitoring the stress conditions, but the proposed models lack implementation and validation^{18,49}. In 2016, Sahraei et al used a model of a Representative Volume Element (RVE) of a cell and proposed a failure model based on simulations of deformation and failure of layers of electrode-separator assembly under various complex loading scenarios. They verified this model for two load cases. However, that model had remained unvalidated to this date as well⁵⁰. A summary of the above studies has been presented in Table 1. One may see under validation section three different notations, V: meaning validated, RC: meaning recalibrated for prediction, which in essence means no universal validation, and N: meaning no validation simulation was performed. It can be observed that to the author's knowledge, no published work in literature before the present work has been validated in all the loading scenarios without recalibration of the failure parameters in different loading cases.

1.3 Failure model development

The objective of this research is to calibrate the Sahraei failure model with homogenous modeling for different types of Li-ion battery cells, validate with different cells under different circumstances. To achieve that, materials of components must be calibrated. Material property and failure behavior of the shell casing of cylindrical cells has been

calibrated from Zhang 2015's work⁴⁴, which we used here and built up the material model in LS-DYNA and RADIOSS in section 3. Material of the jellyroll for through-thickness direction calibration can be found in Sahraei's 2013 work⁵¹. For this study, modeling of the axial property of the jellyroll will be discussed in section 3. The general idea of Sahraei failure model of the jellyroll came from Sahraei's 2016 work⁵⁰; further calibration and validation can be seen in section 3&4. Eventually we need to develop, calibrate and validate our failure criteria under different temperatures, State of Charge (SoC), strain rate and aging effects.

1.4 Effects of temperature, SoC, strain rate and aging

1.4.1 Effects of temperature

Temperature has a significant impact on the performance and lifespan of Li-ion batteries. Capacity will be reduced at both extremely high and low temperatures. At low temperatures (below 0°C or 32°F), the chemical reactions within the battery slow down, reducing the amount of energy that can be delivered. At high temperatures (above 40°C or 104°F), the capacity can degrade due to accelerated chemical reactions, which can cause irreversible damage to the battery. Temperature affects the efficiency of a Li-ion battery. The internal resistance of the battery increases at low temperatures, leading to energy losses and reduced performance. At high temperatures, increased self-discharge rates can also reduce overall efficiency. Frequent exposure to high temperatures can significantly reduce the lifespan of a Li-ion battery. It accelerates the degradation of the electrode materials and electrolyte, leading to capacity loss and decreased cycle life. Excessive heat can even cause thermal runaway, which can result in catastrophic failure⁵²⁻⁵⁷.

Charging a Li-ion battery at temperatures below freezing can cause lithium plating on the anode, which can be dangerous and decrease the battery's lifespan. Charging at high temperatures can lead to capacity fading and can be harmful to the battery's health. High temperatures can also accelerate self-discharge rates, which means the battery will lose charge more rapidly when not in use. This can be a concern for devices or applications that are often in standby mode. Extreme temperatures, particularly high temperatures, can pose safety risks. Li-ion batteries can overheat and, in the worst case, catch fire or explode when exposed to extreme heat. Many Li-ion batteries are equipped with safety mechanisms to prevent such incidents, but there is still a risk ⁵⁸⁻⁶⁰.

Mechanical failure and short circuits will also be affected by temperature. For 18650 cylindrical cell from -40°C to 60°C, the peak force at failure has a 50% difference under rod indentation⁶¹.

Table 1 Contribution comparison with previous works

		Cylindrical/ Elliptical cell							
		Failure criteria for jellyroll		Validation of Failure Criteria with One Set of Parameters V: validated, RC: recalibrated, and N: no validation simulation					
	Model type	Homogenized (H) Detailed (D)		Rod indentation	Hemispherical indentation	Flat compression	Three-point bending	Axial compression	
Sahraei 2012 ¹⁴	Full cell	H	Tensile stress cut off value	V	V	N	N	N	
Greve 2012 ¹⁸	Quarter cell	H	Stress-based (Universal)	N	N	N	N	N	
Wierzbicki & Sahraei 2013 ²¹	Full cell	H	Tensile stress cut off value	V	V	N	N	N	
Wierzbicki & Sahraei 2013 ²¹	Full cell	H	Maximum tensile strain at failure	RC	RC	N	N	N	
Sahraei 2015 ⁴⁸	Full cell	H	Double shear stress-based (Universal)	N	N	N	N	N	
Xu 2015 ¹⁰²	Full cell	H	Maximum tensile strain at failure	RC	RC	N	N	N	
Sahraei 2016 ⁵⁰	Full cell	H	Maximum tensile strain at failure	N	V	RC	N	N	
Sheikh 2018 ⁵⁵	Full cell	D	Maximum tensile strain at failure (Component)	RC	N	RC	RC	N	
2018 ²⁶	Full cell	D	Maximum tensile strain at failure (Component)	V	N	V	V	V	
Wang & Xu 2019	Full cell	H	Triaxiality-based (Component)	RC	RC	RC	RC	N	
Gilaki 2021 ⁶¹	Full cell	H	Maximum tensile strain at failure	RC	RC	RC	RC	N	
Song 2022 ⁴⁵	Full cell	H	Maximum tensile strain at failure	RC	RC	RC	RC	RC	
This work	Full cell	H	Sahraei failure (Universal)	V	V	V	V	V	
		Pouch cell							
		Failure criteria for jellyroll		Validation of Failure Criteria with One Set of Parameters V: validated, RC: recalibrated, and N: no validation simulation					
	Model type	Homogenized(H) Detailed(D)		Medium Hemispherical indentation	Small Hemispherical indentation	Flat compression	Rod indentation	In-plane compression	Three-point bending
Sahraei 2014 ⁵¹	Full cell	H	Maximum principal strain(simple)	V	V	N	N	N	N
Zhang 2015 ¹⁰³	Quart Cell	D	Separator Strain-based	V	V	N	N	N	N
Zhang & Xu 2017 ¹⁰⁴	Full cell	H	Strain-based with damage	N	N	N	N	N	N
Chung 2018 ³⁷	Full cell	H	Stress-based	RC	RC	N	RC	N	N
Keshavarzi 2022 ²⁵	Full cell	H	Maximum tensile strain at failure	RC	RC	RC	RC	RC	RC
This work	Full cell	H	Sahraei failure (Universal)	V	V	V	V	V	V

1.4.2 Effects of SoC

State of Charge (SoC) refers to the current charge level or the amount of energy stored in a lithium-ion (Li-ion) battery, typically expressed as a percentage. The capacity of a Li-ion battery is directly related to its SoC. A fully charged battery has 100% SoC and provides its maximum capacity, while a battery with a lower SoC will deliver a proportionally reduced amount of energy. Voltage of a Li-ion battery is also affected by its SoC. As the SoC decreases, the voltage also decreases. Monitoring the voltage can be a way to estimate the SoC, and this information is crucial for various battery management systems and applications. Li-ion batteries tend to have a longer cycle life when they are operated within moderate SoC. Operating a battery continuously at high or low SoC levels can lead to accelerated degradation and reduced overall lifespan^{33,62–68}.

Overcharging and over-discharging can be dangerous for Li-ion batteries. Managing the SoC within safe limits is critical to prevent overcharging, which can cause thermal runaway, or over-discharging, which can damage the battery or even lead to safety hazards. The performance of a Li-ion battery, such as its ability to deliver power, can be affected by the SoC. Some applications may require a certain SoC to operate optimally. For example, electric vehicles often perform best when the battery SoC is maintained within a certain range^{2,69–73}.

1.4.3 Effects of strain rate

Strain rate effects can be important in the mechanical behavior of materials, including Li-ion batteries. However, the significance of strain rate effects on Li-ion batteries largely depends on the specific materials and designs used in the battery. Li-ion batteries are

typically housed in rigid casings or enclosures. The mechanical integrity of these casings is important for battery safety. Under certain conditions, such as impact or crushing, the strain rate (rate at which the material deforms) can affect the behavior of the battery. A higher strain rate, such as that caused by a sudden impact, can lead to different deformation responses compared to slower deformation^{63,64,74}.

The strain rate effects may vary depending on the type of Li-ion battery. Pouch cells, which are commonly used in consumer electronics, are often more susceptible to deformation and swelling under mechanical stress, and the strain rate can impact how these cells behave when subjected to external forces. Cylindrical and prismatic cells, covered with a strong metal casing, are generally more robust and less sensitive to strain rate effects^{30,66,75,76}.

Inside the battery, the anode, cathode, separator, and electrolyte materials can have different mechanical properties and strain rate sensitivities. The relative movement and deformation of these components under different strain rates can affect the overall performance and safety of the battery. Li-ion battery manufacturers and designers take strain rate effects into account when designing safety features. These may include mechanical safeguards, such as reinforcing the battery casing or using materials that can absorb and dissipate mechanical energy to protect the internal components^{30,55,62,68}.

1.4.1 Effects of aging

During the whole battery lifespan, due to charging and discharging, the degradation of cell components is known as aging. Aging has been extensively studied in the context of electrochemical performance, but its impact on mechanical behavior is increasingly gaining attention due to the rising importance of battery safety, especially under abuse

conditions. As the cell ages, physical and chemical transformations will significantly change the structural integrity and mechanical response⁷⁷.

The first effect of aging is the loss of material strength and ductility. In Wu et al 2017's study, anode, cathode and separator after aging shows this effect⁷⁸. In this study, all components are tested with fresh sample and aged sample, under compression, tension and indentation. All components show material deterioration. Among all components, anode has the most deterioration affected by aging where separator has the least impact. Cathode has also been found that get more brittle and easy to obtain fracture after charging⁷⁹. In Zhang et al 2017's study, a more specific study for aging impact on separators has been reported. The material strength of the separator shows degradation due to cell cycles, thus, the maximum force for the full battery cell to get short circuit under mechanical abuse is also decreased after cycling³.

Another effect is the structural integrity of the cell. Electrodes will swell due to cycling, for cylindrical cell, the expansion of electrodes will cause internal stress accumulation when the electrodes reach the metal can. Stress concentration will then happened at non-uniform geometry location and cause buckling, metal inside anode and cathode will then penetrate the separator and cause short circuit⁸⁰⁻⁸³.

CHAPTER 2

METHOD

2.1 Introduction

This section will first introduce all batteries used in this research, including the geometry and electrical properties. Then the experiments conducted will be discussed. The RVE based failure model is also included in this section.

2.2 Battery Specification

Two commercial 18650 cylindrical cells and one commercial pouch cell were used for model calibration and validation. The first cylindrical commercial cell, here referred to as Cell A, had lithium cobalt dioxide (LCO) chemistry, with 2,600mAh capacity and 3.7 V normal voltage¹⁴; and a second cylindrical commercial cell, here referred to as Cell B, with lithium-iron-phosphate (LFP), had 1500mAh nominal capacity and 3.2 V average capacity. A full cylindrical cell model here contained two parts: shell casing and jellyroll. Each part had been previously characterized and associated homogenized models were calibrated to have good prediction of load-displacement and shape of deformation under lateral and axial loadings as well as three-point bending^{43,46}. In this paper, the models were updated to use the /FAIL/SAHRAEI failure criteria for fracture of the jellyroll. The full failure locus for each cell was calibrated by using the failure strain and strain ratios for individual loading cases.

The pouch cell used in this study was a commercial cell with NMC chemistry used commonly in a manufactured electric vehicle. This pouch cell has a geometry of 11.43*110*310 (Thickness*Width*Length in mm). The nominal capacity and voltage are

60Ah and 3.68 V. Discharge cut-off voltage for this cell is 3 V. Compared with cylindrical cells, pouch cell doesn't have the metal shell casing, it only uses a very thin polymer pouch to carry the cell, which means the whole cell can be homogenized in one part. The pouch cell model also was similarly coupled with a /FAIL/SAHRAEI criterion which was calibrated to predict the failure in all loading cases.

2.3 Experiments

Here we provide a short summary of the experiments available for each of these cells from the previous work of the authors^{15,46} as well as new experiments performed for the current study. Five tests were done for both cell A and cell B: rod and hemispherical indentation, flat compression, three-point bending and axial compression. Both cylindrical cells were fully discharged before conducting the experiments. Cell A was tested on a MTS load frame with displacement control and a 10 kN load cell, using a Radio Shack Digital Multimeter for voltage measurement¹⁴. Experiments of cell B and pouch cell were performed on an Instron 5985 load frame with 250 kN load cell. LVDT deflection sensor (model 2601-043) was also used to ensure the accuracy of the displacement measurement⁴⁶. For all tests, displacement was applied at 1 mm/min rate, except for cell B's three-point bending test, where a 0.25mm/min rate was used to get better observation of the fracture. All tests are performed twice to ensure repeatability. Six tests were performed for the pouch cell, including 2 different hemispherical indentations, rod indentation, flat compression, three-point bending and in-plane compression test. Batteries were charged and discharged for 5 cycles and were tested with 0% state-of-charge. Experiment data for all cells were summarized in Figure 1, a brief explanation of each test scenario is included below.

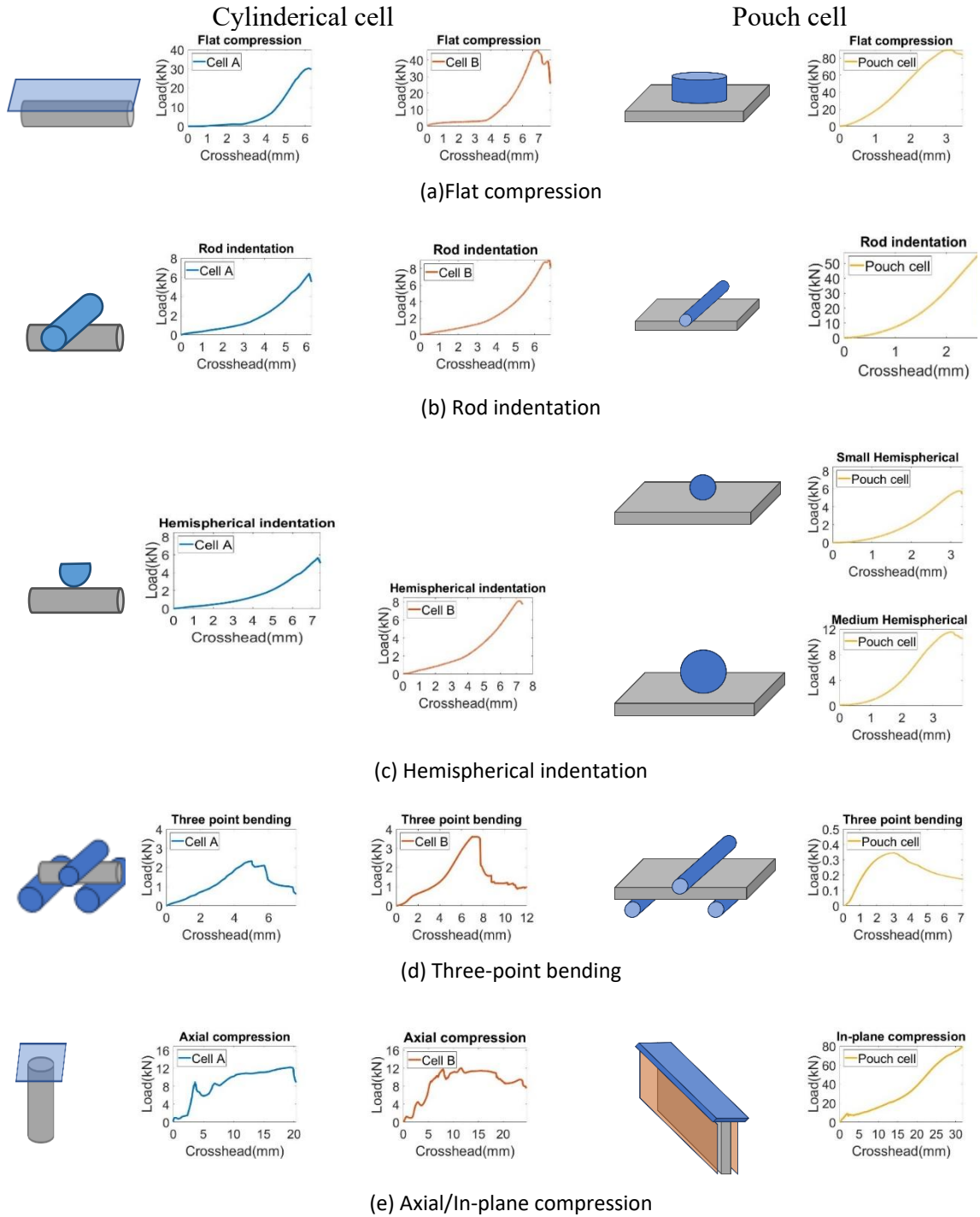


Figure 1 Experiment schematics and results

2.3.1 Flat Compression

In the compression tests, a battery cell was laid on a fixed flat plate and compressed by a moving flat platen on the top. Cell A has a 30 kN peak force at 6 mm displacement; cell B has a 45 kN peak force at 6.8 mm displacement, see Figure 1(a). The cell was packed into a plastic bag for safety protection. For the pouch cell, since the cell has a large geometry, test force will be too high if the full surface of the cell is compressed. Therefore, a flat cylindrical punch has been used for the pouch cell. The diameter of the punch is 40 mm. Pouch cell has a peak force of 90 kN at 3 mm displacement, see Figure 1(a).

2.3.2 Rod indentation

In this test, the cell was placed on a flat plate and indented by a rod indenter. There is a slight difference between cell A and cell B's rod indentation. The rod indenter is about 16 mm in diameter. The peak force of cell A is 6.4 kN at displacement 6.3 mm; cell B has a 9 kN peak force at displacement 6.5 mm. The rod indenter for pouch cell is also 16 mm diameter, and the peak force is around 60 kN with 2.7 mm displacement. See Figure 1(b) for a summary of all rod indentation tests.

2.3.3 Hemispherical indentation

Both cell A and cell B are using a 12.7 mm hemispherical indenter for this test. For cell A, 5.8 kN peak force was obtained at 7.4 mm displacement; for cell B, 8.1 kN peak force was obtained at 7.2 mm displacement, see Figure 1(c).

Two different hemispherical tests were performed for the pouch cell, the small one used a 12.7 mm diameter where the medium one had 25.4 mm diameter hemispherical indenter.

Small hemispherical test had a 5.9 kN peak force at 3.2 mm displacement; the medium one had 11.8 kN at 3.5 mm displacement, see Figure 1(c).

2.3.4 Three-point bending

The three-point bending test fixtures were different for each of the cells. Cell A was bent between two supporting beams with 48 mm diameter, and the top indenting rod punch had a 10 mm diameter, the distance between two supporting beams was 58 mm. For cell B, the cell was bent between two supporting beams with 16 mm diameter, and top punch had the same size with the supporting beam, the distance between two supporting beams was 48 mm. Cell A had a 2.4 kN peak force at displacement 5.3 mm, Cell B had a 3.65 kN peak force at displacement 7 mm, see Figure 1(d). It should be noted that while for transverse loading cases such as rod indentation, hemispherical indentation, and compression between two flat plates, the force drop is due to jellyroll failure. For three-point bending, the first drop of the force is due to buckling of the shell casing; then another drop of force is based on shell casing failure, and the last drop is because of jellyroll failure.

For the pouch cell, the top rod indenter and two supporting beams had the same diameter of 16 mm and the distance between two supporting beams was 140 mm. The peak force of 0.35 kN happened at 3 mm displacement. Force drop after the peak was due to a hinge formed in the middle of the cell, but there was no short circuit obtained for this test.

2.3.5 Axial/In-plane compression

Axial compression tests were performed for each cylindrical cell between two flat plates, see Figure 1(e). For cell A, end caps were removed to have a flat surface on two sides of the cell. Cell A had a 9 kN peak force at 4 mm displacement, then the buckling

happened for the shell casing which caused the force to drop to 6 kN before eventually increasing again to 12 kN. Cell B had a 12 kN peak force at 8 mm displacement before buckling and then dropped to 9 kN before increasing to 12 kN at the end of the experiment.

For the in-plane compression test on the pouch cell, a confined set up was used, where the cell is held between rigid flat plates on the large surfaces during in-plane loading. The punch compression applied to the thickness of the cell continues until it has traveled approximately one-third of the cell's vertical length, approximately 33 mm here. No force drop was obtained during the whole procedure for the pouch cell.

2.4 RVE based Sahraei failure model

In 2016, Sahraei et al used computational homogenization to simulate deformation and failure of a RVE for an elliptical cell. This method is a numerical technology used to simulate the homogenous behavior of multi-materials structures by considering the properties of microstructure⁸⁴⁻⁸⁶. The interior of battery cells is made of different material layers including anodes, cathodes, metal current collectors and separators. The RVE is the smallest unit that repeats in the cell and can make the whole cell. Homogenization provides the possibility to obtain jellyroll behavior in macro-scale based on the response of the various interior components in micro scale. In the absence of body forces, the mechanical equilibrium for micro- and macroscale can be written as:

$$\nabla P_m = 0, \text{ in } V, \text{ RVE volume.} \tag{1}$$

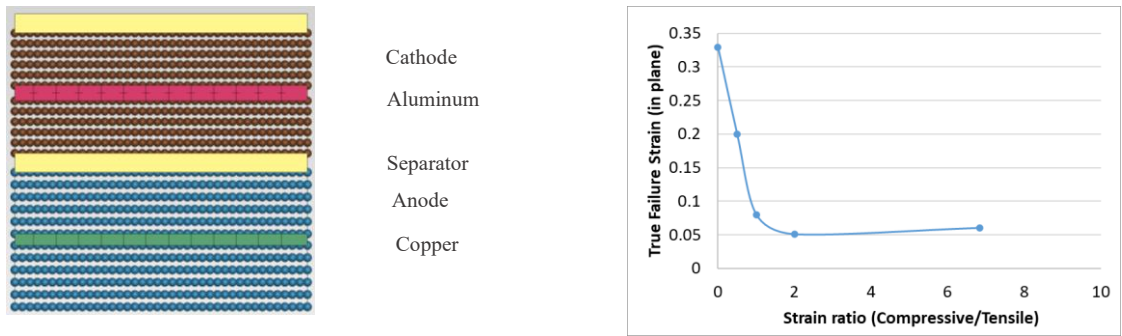
$$\nabla P_M = 0, \text{ in } V_0, \text{ Domain volume.} \tag{2}$$

Here, P_m is the first Piola-Kirchhoff stress tensor in microscale; P_M is the first Piola-Kirchhoff stress tensor in macroscale. The relation between micro- and macroscale stress tensor can be written as^{32,50}:

$$P_M = \frac{1}{V_0} \int_{V_0} P_m dV_0 \quad (3)$$

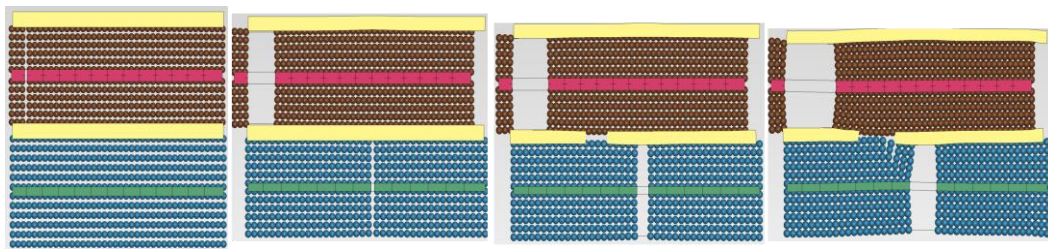
Sahraei et al⁵⁰ developed a micro-scale RVE for the battery cell by modeling each component of the electrode-separator assembly individually, see Figure 2(a): separator (yellow color), copper and aluminum (red/green color), coating of the electrodes (blue/brown color). The porous anode and cathode coatings were modeled with crushable foams, while the metal current collectors were defined by piecewise linear plasticity models. The separator was modeled with a combination of crushable foam behavior under compression and a plasticity model under tension. Each layer was assigned its material and failure properties based on its own response observed in single layer tensile/compressive and biaxial testing⁵⁰. The thickness of the separator was 20 μm and its failure criterion was a principal tensile failure of 0.33 mm/mm. The aluminum foil layer was 16 μm and was assigned a failure value of 0.049 equivalent plastic strain. The copper layer was 9 μm thick and was assigned a 0.178 equivalent plastic strain. For the details of the material data for each layer of the model, readers are advised to review the reference paper by Sahraei et al⁵⁰. The RVE consisting of the layers of electrode-separator assembly was then used to simulate deformation and failure under a combination of through-thickness compression/tension and in-plane tension loads. A failure locus was plotted based on simulation of five different cases of through-thickness in-plane strain ratios, ranging from pure in-plane tension with no through-thickness compression to pure through-thickness

compression with no applied in-plane tension, See Figure 2(b). Kermani et al later added simulation of in-plane compressive loads with a similar but longer RVE⁸⁷. These studies showed that under pure in-plane tension, there is no interaction between different layers of the RVE, therefore, short circuit is due to failure of the separator at a strain value equal to that of the separator itself, which is 0.33 mm/mm, see Figure 2(b). When compression between the layers increases, the interaction between the layers increases as well. Therefore, the early failure of current collectors will localize the deformation of separators and lead to an early failure of separator, causing short circuit at tensile strain values of about 0.05 mm/mm. Figure 2(c) and 1d show the sequence of failure of layers under combination of tensile and compressive loads, while in Figure 2(c), they are dominantly tensile versus in Figure 2(d) they are mostly compressive. In cases of through-thickness tension, the layers just separate from each other, and no short circuit will be initiated. Also, in-plane compression ultimately causes buckling of the layers but does not lead to short-circuit or causing fracture in the layers. Pure shear also just causes sliding of the layers over each other with no failure.

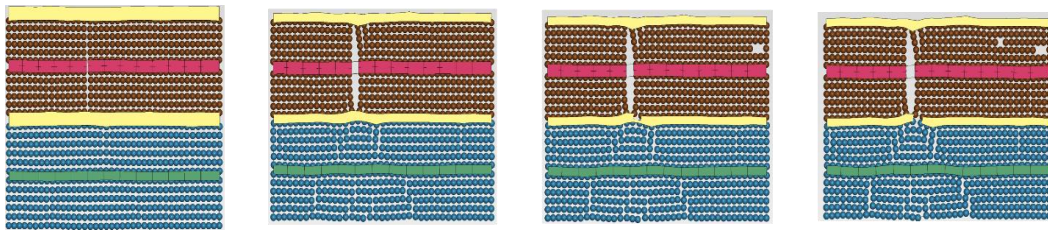


(a) Original RVE model

(b) Five different cases of through-thickness in-plane strain ratios.



(c) RVE failure with tension dominated.

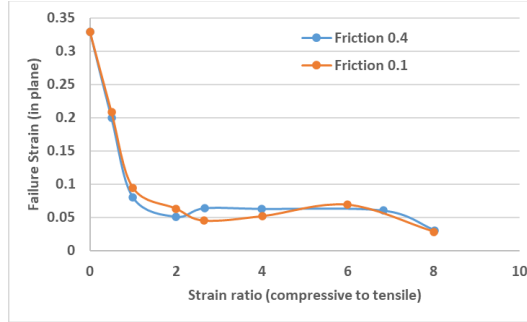


(d) RVE failure with compression dominated

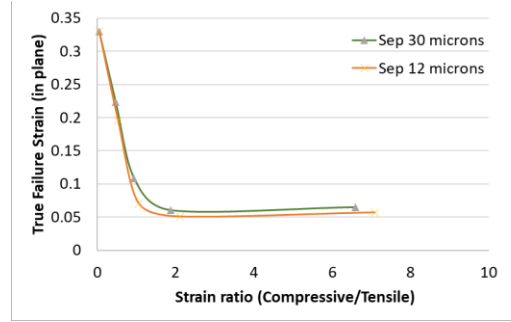
Figure 2 Sahraei 2016 model failure strain versus ratio of compressive to tensile strain

To further understand the failure response of this RVE, additional simulations were performed in this work. In a first attempt, additional strain ratios were simulated to generate a total of eight points for the failure locus to make sure the function will not behave significantly differently in the ranges of strain ratios that were not modeled previously. Then, to understand the effects of friction between the layers, two extreme cases of friction of 0.1 and 0.4 were simulated for all the above cases. Figure 3(a) shows the failure locus for all the simulated cases with the two friction values. These simulations showed similar trends with minimal changes for all load cases, hence confirming the stability of this failure locus as a function between the two identified variables. To verify how changes in a separator layer can affect the failure locus, additional simulations were performed for an RVE with a separator thickness of 30μ and 12μ . These values were chosen based on the thickness of commercially available separators on the market. To verify effects of current collector failure, additional simulations were performed with aluminum current collectors of 12μ and 20μ thickness. This variation again was chosen based on commercially available aluminum current collectors on the market. Figure 3(b), and Figure 3(c) show the observed changes in the failure locus based on the variations in the layers' properties above. The main purpose of these simulations was to observe the effects of changes in each of the layers on the final shape of the failure locus. It can be observed that a thicker separator may not have any significant effects on the failure locus, as the lower section of the failure locus is limited to the failure of the aluminum current collector. The reduction in the thickness of the current collector however reduces the contribution of its strength. Therefore, at the onset of failure of current collector, a smaller shock is transferred to adjacent layers and the localization of deformation in the separator is delayed. This change raises the lower

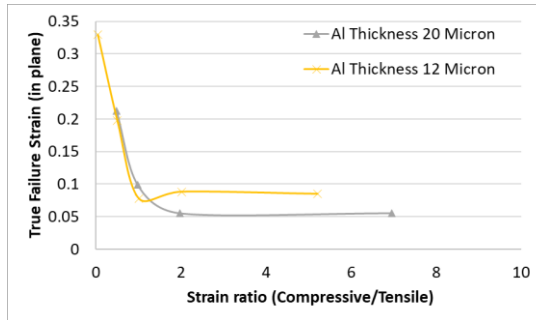
limit of failure strain for the RVE with a thinner aluminum current collector. The above simulations show that the RVE Based failure locus can connect the response of the microstructure of the cell to its homogenized failure properties. In the next step, one needs to evaluate whether this failure locus can predict the failure in full cell homogenized models.



(a) 8 different simulations with 0.1/0.4 friction



(b) 8 different simulations with 12/30 microns separator thickness



(c) 8 different ratio simulations with 12/20 microns Al current collector thickness.

Figure 3 Sequence of different loading and failure of the RVE

CHAPTER 3

COMPUTATIONAL MODELING

3.1 Introduction

In this section, homogenous models for two cylindrical cells and one pouch cell will be built up, to do simulation in commercial software RADIOSS and LS-DYNA. For cylindrical cells, both shell casing and jellyroll material will be discussed while for pouch cell there is only jellyroll material.

3.2 18650 cylindrical cell model

3.2.1 Shell casing material

The shell casing is the main cell level protection for an 18650 Li-ion cell. The manufacturing procedure of the shell casing is through deep drawing which usually causes anisotropy and a non-uniform thickness at different locations on the shell casing ⁸⁸. However, for modeling purposes, we consider a uniform average thickness throughout the casing. The dimensions of the shell casing are 65 mm in length, 18 mm in diameter, and 0.26mm in thickness. The manufacturing procedure will cause anisotropy in the metal sheet which is formed into a cylindrical shell casing as a cylinder. Zhang and Wierzbicki performed a detailed analysis and modeling of cylindrical shell casings in 2015 ⁴⁴. Following that work, for plane stress cases, the Hill48 can be simplified as:

$$\sigma_1^2 + \frac{R_0(1 + R_{90})}{R_{90}(1 + R_0)} \sigma_2^2 - \frac{2R_0}{1 + R_0} \sigma_1 \sigma_2 = (\sigma_1^y)^2$$

(4)

Here R_0 , R_{45} and R_{90} represent the r values in different angles from the rolling direction. To obtain the stress-strain hardening curve, Zhang and Wierzbicki 2015 used a window shaped specimen cut from the shell casing to avoid flattening effect. Post necking behavior was calibrated by using a combination of Swift and Voce laws:

$$\begin{aligned}\sigma &= aA_s \varepsilon^{n_s} + (1 - a)(B - C * \exp(-D * \varepsilon)) \\ &= 400\varepsilon^{0.084} + 0.5(356 - 194.5 * \exp(-360 * \varepsilon))\end{aligned}\tag{5}$$

Where a , A_s , n_s , B , C , and D are all constant parameters of the fit for the shell casing hardening curve, see Table 2⁴⁴.

Table 2 Parameters for combined Voce-Swift law and the fracture locus

a	A_s	n_s	B	C	D	
0.5	800	0.084	356	194.5	360	
c_1	c_2	c_3	A	$1/n$	A_j	n_j
0.2	425MPa	0.9	680MPa	0.047	550Mpa	2

3.2.2 Shell casing failure model

For uniaxial loading, strain-based or stress-based failure criteria can perform well with a lower cost, however when loading becomes complicated, i.e. three-point bending, the precision on prediction of cracks will be a major problem^{39, 27}. Among previous work on modeling fracture of battery shell casings, Modified Mohr-Coulomb (MMC) has been found to perform well on prediction of crack under various load conditions^{44,89-93}.

To implement MMC, a damage indicator, $\Delta D(\bar{\varepsilon}_f)$, is used as a function of the plastic strain $\bar{\varepsilon}_p$.

$$\Delta D(\bar{\epsilon}_f) = \int_0^{\bar{\epsilon}_p} \frac{d\bar{\epsilon}_p}{\hat{\epsilon}_f(\eta, \bar{\theta})} \quad (6)$$

$\hat{\epsilon}_f(\eta, \bar{\theta})$ is the fracture locus for the material. The fracture locus was introduced in Bai and Wierzbicki's 2008 paper as a 3D surface generated for plastic strain at failure as a function of triaxiality and lode angle parameter dependence.

$$\hat{\epsilon}_f(\eta, \bar{\theta}) = \left\{ \frac{A}{c_2} \left[c_3 + \frac{\sqrt{3}}{2 - \sqrt{3}} (1 - c_3) \left(\sec\left(\frac{\bar{\theta}\pi}{6}\right) - 1 \right) \right] \times \left[\sqrt{\frac{1 + c_1^2}{3}} \cos\left(\frac{\bar{\theta}\pi}{6}\right) + c_1 \left(\eta + \frac{1}{3} \sin\left(\frac{\bar{\theta}\pi}{6}\right) \right) \right] \right\}^{-\frac{1}{n}} \quad (7)$$

$c_1, c_2,$ and c_3 are fracture locus parameters that must be determined from experiments. A and n are the parameters of a power law fit for the hardening curve of the material, see Table 2. Zhang and Wierzbicki, 2015, did five different experiments to determine different parameters and get the fracture locus for a battery shell casing following Luo's work^{44,94}. Using the values calibrated by these authors, Equation 7 becomes:

$$\hat{\epsilon}_f(\eta, \bar{\theta}) = \left\{ \frac{680}{425} \left[0.9 + \frac{\sqrt{3}}{2 - \sqrt{3}} (1 - 0.9) \left(\sec\left(\frac{\bar{\theta}\pi}{6}\right) - 1 \right) \right] \times \left[\sqrt{\frac{1 + 0.04}{3}} \cos\left(\frac{\bar{\theta}\pi}{6}\right) + 0.2 \left(\eta + \frac{1}{3} \sin\left(\frac{\bar{\theta}\pi}{6}\right) \right) \right] \right\}^{-0.047} \quad (8)$$

3.2.3 Jellyroll material

The jellyroll includes all the layers of electrodes, separator assembly, wound inside the cylindrical shell casing. The advantage of a homogenous material model for the jellyroll, where the properties of all of its' components are combined, is a significantly lower simulation cost compared to detailed modeling. As a result, such a model can be used in model-based design analysis for optimization and evaluation of battery packs and

protective structures ⁴⁶. Yet, the most important feature for a homogenized model is its accuracy in predicting a variety of complex loading cases. No single homogenized model presented in the literature has been capable of simulating the response of a cylindrical cell under lateral indentation, three-point bending, and axial compression with one set of material calibration. The main reason for that is rooted in the highly anisotropic material behavior of a jellyroll due to its multi-layer multi-material set-up embodying both structural and material anisotropy. In this study, two different material models have been used and compared to evaluate their capabilities and shortcomings in the prediction of the above desired features. The first material used is a commonly used crushable foam with isotropic behavior, and the second one includes an anisotropic honeycomb model.

Sahraei et al. 2012 proposed using an uncoupled crushable foam model for simulation of lateral indentation of cylindrical cells ¹⁴. The model does not follow the well-known plasticity concepts such as traditional flow rules. Instead, the response is decoupled in the three directions of principal stresses. A hardening curve is defined for the response of the cell under compressive principal stress, and a tensile cut-off value is given for the tensile principal stresses. The elastic response of the material follows Young's modulus equal to the highest slope of the compressive hardening law. Sahraei et al. proposed a power law hardening curve for this isotropic material model as:

$$\sigma = A_j \epsilon^{n_j} = 550 \epsilon^2$$

(9)

Where A_j and n_j are the constants of the jellyroll hardening¹⁴. This model can predict the lateral compression and three-point bending for the jellyroll but has not been validated

for axial compression. In the current study, this model will be evaluated for axial compression prediction in addition to the previous loading cases.

Sahraei et al. later used an anisotropic material model in 2015⁴⁸. This model also behaves uncoupled in three directions. However, those directions come from the principal directions of anisotropy of the material rather than the principal stresses. In this model, the compression and tension are calibrated separately in each principal direction of material anisotropy. Therefore, using this material model, in addition to the compressive response, the authors calibrated the tension stress-strain relations in three directions of anisotropy, using test data at cell and component levels⁴⁸. This model showed advantages over the isotropic model in prediction of the lateral indentation for a cell with central mandrill and is superior to the isotropic model in prediction of anisotropic failure and crack in the jellyroll. The tension calibration in this model includes two steps. In the first step, the average response of the multi-layer electrode-separator assembly is calculated from tests on each of the layers as:

$$\sigma_{average1} = \frac{\sum \sigma_i t_i}{\sum t_i} \quad (10)$$

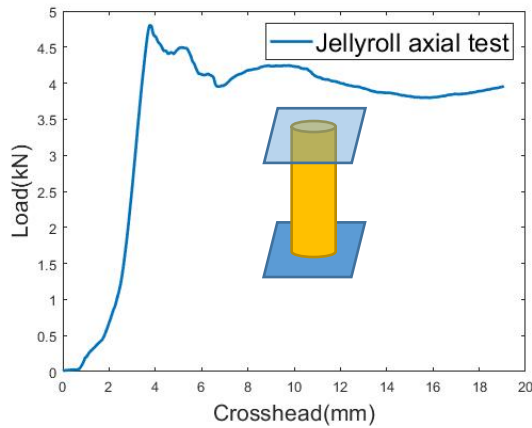
Where $\sigma_{average1}$ is the homogenized tensile response in step one, σ_i represents the stress in each layer of the assembly, i.e. aluminum and copper foils, active coatings, and separator, and t_i represents the corresponding thickness of the layer. The curve calculated from this method has several softening steps, due to failure of each of the layers and transfer of loads on the remaining components. To avoid instability in the model due to these consecutive failures, a second step is used, by converting the average tensile curve into a

power law hardening equivalent which has the same level of energy absorption during deformation, using:

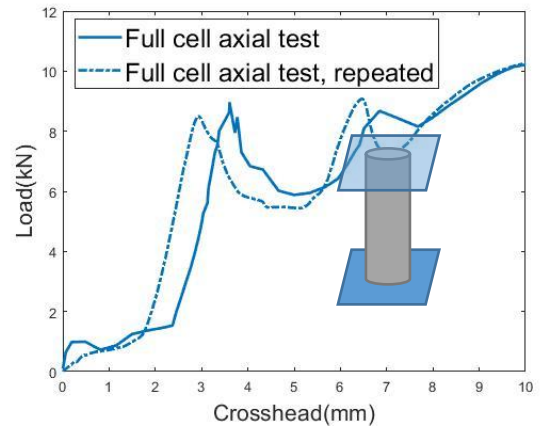
$$E = \int_0^{\varepsilon_f} \sigma_{average2}(\varepsilon) d\varepsilon = \int_0^{\varepsilon_f} A_t \varepsilon^{n_t} d\varepsilon \quad (11)$$

Where $\sigma_{average2}$ is the homogenized tensile response in step 2, and A_t and n_t are the parameters of the tensile hardening curve. This method was used in the two directions of separator anisotropy, Machine Direction (MD) and Transvers Direction (TD). They proposed using a shear response that is symmetric in tension and compression and is equal to half of the normal compression strength⁴⁸. The authors validated this model under two loading cases, lateral indentation with a rod, and a hemispherical punch. In the current study, the above model is extended with a refined calibration to simulate these additional loading cases. The most important property for these cases is the hardening curve in axial direction of the jellyroll. Previous studies have shown that the in-plane compression strength of the cell is higher than the through-thickness strength by a constant increase, equal to the buckling strength of aluminum and copper foils^{42,95}. The foils do not have any significant contribution to the strength when they are in series with softer components such as active coatings and separators in through-thickness compression; but their role becomes important when they are in parallel with other components, such as in-plane loading cases. Therefore, in the current study, the in-plane compression hardening curve is calculated from an axial compression test on a jellyroll without shell casing see Figure 4(a). The test shows an increase in force up to 4,000 N, which is the buckling strength for the jellyroll under axial compression. From this value, the buckling stress is estimated to be 20 MPa. The in-plane strength of the jellyroll after buckling cannot be directly extracted from the

axial compression curve because of the loss of stability after buckling. However, previous studies show that the response after buckling should be parallel to the through-thickness strength of the curve. Therefore, the full in-plane compression curve is built by adding the 20 MPa buckling strength to the through-thickness compression curve.



(a) Force-displacement result for jellyroll only with schematic



(b) Force-displacement result for full cell with schematic



(c) Jellyroll deformation mode



(d) Full cell deformation mode

Figure 4 Axial compression of the cylindrical cell

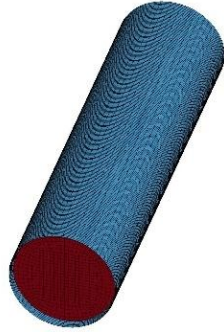
In general, temperature and voltage are two main factors interconnected with the mechanical integrity of the battery. When inside of the Li-ion battery has a fracture, a force drop also can be observed and a short circuit may be initiated immediately. Usually this is accompanied by a drop in voltage and a rise in temperature. In this study, the maximum principal strain has been used to define failure for the isotropic crushable foam model. For the anisotropic honeycomb material, a maximum tensile strain is used as the failure criterion for the jellyroll. A failure in the test is considered at the onset of force drop. In the cases of experiments that voltage was also measured, the force drop has consistently been coinciding with a drop in voltage, indicating the development of an electric short circuit with mechanical failure¹⁴.

3.2.4 Finite element modeling of Shell Casing and jellyroll

The cell model is composed of two parts, a jellyroll, and a shell casing, following the measurements of the actual cell, see Figure 5. The model of shell casing was developed assuming a uniform thickness of 0.26 mm along with the casing, ignoring the variations in thickness due to the deep drawing procedure. Fully integrated shell elements of 0.4×0.4 mm were used. The Young's modulus was defined as 160 Gpa⁴⁴. Hill's anisotropic model was used for shell materials, the 3R values for the shell casing material were given by Zhang and Wierzbicki 2015 as $R_0 = 0.77$, $R_{45} = 0.62$ and $R_{90} = 0.66$, Equation 4 then can be written as follows⁴⁴:

$$\sigma_1^2 + \frac{R_0(1 + R_{90})}{R_{90}(1 + R_0)} \sigma_2^2 - \frac{2R_0}{1 + R_0} \sigma_1 \sigma_2 = \sigma_1^2 + 1.0942 \times \sigma_2^2 - 0.8701 \times \sigma_1 \sigma_2 = (\sigma_1^y)^2$$

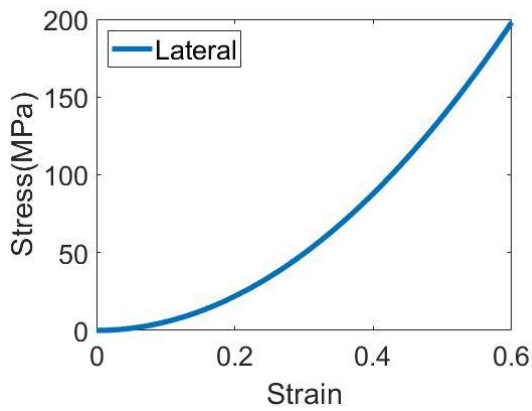
(12)



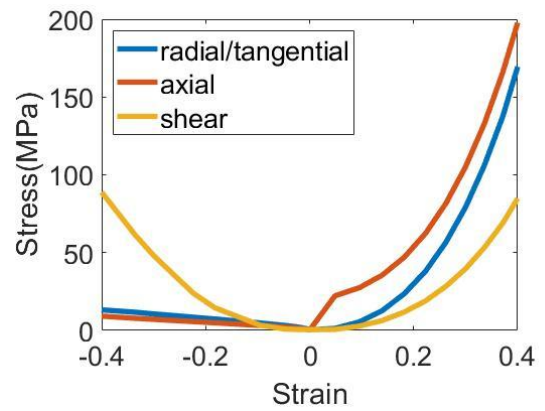
(a) Discretization of the 18650-battery cell without caps.



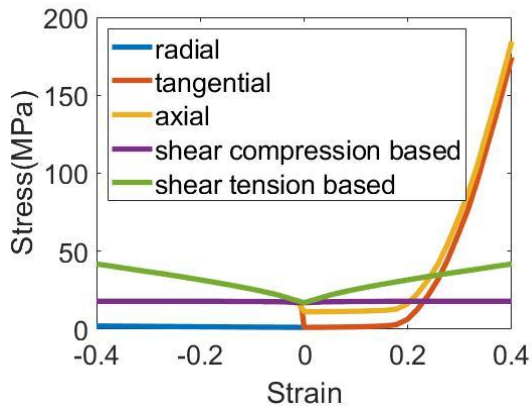
(b) 18650 battery cell without caps



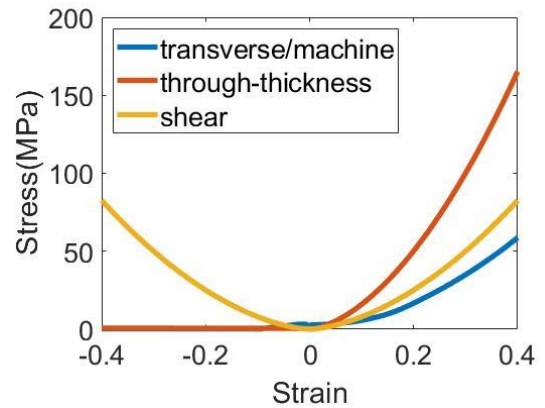
(c) Compressive volumetric stress-strain input curve for crushable foam.



(d) Input curves converted in RADIOSS for cell A



(e) Input curves converted for RADIOSS in cell B



(f) Input curves converted in RADIOSS for pouch cell

Figure 5 FEM model and material inputs for isotropic/anisotropic of the jellyroll

The hardening curve for this material was constructed for material input using the parameters of combined Voce-Swift law, see Table 3. To implement the MMC fracture in LS-DYNA, Generalized Incremental Stress State Dependent Damage Model (GISSMO) feature was applied. The parameters for the fracture locus were used to develop the table input for GISMMO, see Table 3.

Table 3 Material properties for cylindrical (cell A and B) cell's jellyroll

Cell A		
Elastic modulus for three directions of anisotropy	Shear modulus for three directions of anisotropy	Young's Modulus for bulk material
500 MPa	250 MPa	79 GPa
Poisson's ratio for bulk material	Yield stress for bulk material	
0.3	200 MPa	
Cell B		
Elastic modulus for three directions of anisotropy	Shear modulus for three directions of anisotropy	Young's Modulus for bulk material
1000 MPa	500 MPa	79 GPa
Poisson's ratio for bulk material	Yield stress for bulk material	
0.3	200 MPa	

3.3 Pouch cell model

3.3.1 Jellyroll material model

The material property and calibration for pouch cell jellyroll is similar to previous section 3.2.3. Input curves can be found in Figure 5.

Table 4 Material properties for pouch cell's jellyroll

Pouch cell		
Elastic modulus for transverse direction	Elastic modulus for machine direction	Elastic modulus for through-thickness direction
2460 MPa	2460 MPa	1290 MPa
Shear modulus for transverse/machine	Shear modulus for machine/through-thickness	Shear modulus for through-thickness/transverse
1230 MPa	50 MPa	645 MPa

In the current project, the models were all moved to the commercial software RADIOSS to couple the material model with the implemented /FAIL/SAHRAEI criterion for predicting failure of jellyroll/electrode stack. The purpose was to evaluate whether using a failure locus based on RVE simulations (/FAIL/SAHRAEI) that defines in-plane tensile failure strain as a function of the ratio of through-thickness compressive strain over in-plane tensile strain can predict the failure in all loading scenarios with one single model. The HyperCrash software from ALTAIR HyperWorks was used for model conversion from LS-DYNA to RADIOSS. The material model used for the jellyroll/electrode stack was /MAT/HONEYCOMB material model in RADIOSS which is equivalent to MAT_HONEYCOMB which was used in LS-DYNA. The rigid indenter parts in LS-DYNA were converted to elastic parts with a rigid designation in RADIOSS. Those conversions were done automatically. However, after the model is converted using HyperCrash, a series of manual changes were also performed to make the model ready for solution by the RADIOSS solver. These included:

Converting the engineering stress-strain curves from LS-DYNA to true stress-strain curves for honeycomb material in RADIOSS. Removing extra copies of the interface and time history cards.

For cells with metal casing that were modeled with Hill's material model in LS-DYNA, the Hill_Tab model in RADIOSS needs to be defined manually.

The Modified Mohr Coulomb (MMC) failure criteria for the shell casing in LS-DYNA needs to be updated to the BIQUAD failure model in RADIOSS.

3.4 Sahraei failure model

We introduced the Sahraei failure in section 2.4. To continue evaluation of this failure criterion, in the current work, a user defined code was implemented in the commercial software RADIOSS. This code, titled Sahraei failure criterion (/FAIL/SAHRAEI), defines the failure of a homogenized jellyroll using the in-plane tensile strain to failure as a function of the ratio of through-thickness compression strain over in-plane tensile strain. Then the model was calibrated for two cylindrical cells, here named cell A and cell B and one pouch cell to verify its capability in predicting failure in various loading cases.

A FORTRAN code is used to define the failure model based on the strain ratio. In the code we define the ε_{11} as the through-thickness direction (x direction in Figure 6), looking for compressive strain; ε_{22} as the hoop direction which is the machine direction of the separator (y direction in Figure 6); ε_{33} as the axial direction which is the transverse direction of the separator (z direction in Figure 6). The ratios are calculated as $c_2 = \frac{\varepsilon_{11}}{\varepsilon_{22}}$ and $c_3 = \frac{\varepsilon_{11}}{\varepsilon_{33}}$. The code will then look for the corresponding failure strain value in each direction of anisotropy (ε_{f2} and ε_{f3}) based on the current strain ratio at each time step. If the plastic strain is greater than the defined failure strain value, the element will then be deleted as an indication of failure. The code works are attached to Appendix A. The governing equation of the failure model can be see below:

$$c_i = \frac{\varepsilon_{11}}{\varepsilon_{ii}} \quad i = 2 \text{ and } 3 \quad (13)$$

$$\varepsilon_{f_i} = f(c_i) \quad i = 2 \text{ and } 3 \quad (14)$$

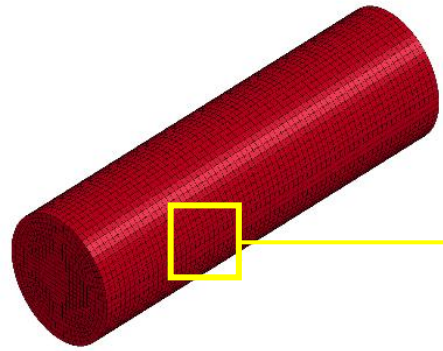
To get the failure curve, we need to run all different loading cases separately, obtaining different failure strain value and the strain ratio value at each loading cases. A curve fitting tool will then be needed to generate a reasonable curve based on the data points. In section 2.4, we have discussed the failure curve shape, that is higher tensile failure strain value when strain ratio is low, lower tensile failure strain value when strain ratio is high.

3.5 Element orientation

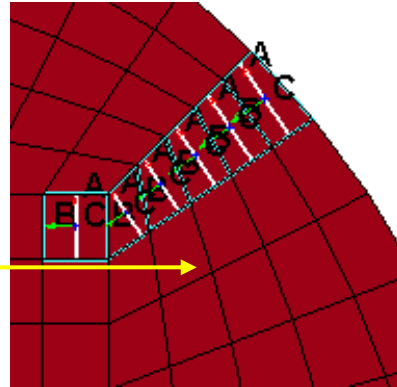
Another important point is that the RVE based criterion is using the strains in three directions of anisotropy of the cell, which are aligned with machine direction, transverse direction and through-thickness direction of the separator. Therefore, a proper coordinate system for identifying the orientation of battery layers is very important for correct application of this failure model. In the previous models, the solid elements' orientations were defined based on the nodes on each element. With a relatively cylindrical mesh, the elements on the exterior of a cylindrical cell could have minimal deviation from cylindrical coordinate system. However, moving toward the center, their orientation was not strictly following the cylindrical coordinate. As it can be seen in Figure 6(b), In the external layers' elements have one radial, tangential, and axial direction, however for center square elements, they get disordered. To fix this issue, a code was written and implemented in the program to re-align all elements to have the same radial, tangential, and axial direction, as seen in Figure 6(d). This alignment makes sure the jellyroll model is getting closer to the

reality where the layers are stacked and rolled up to form a cylindrical jellyroll. It should be noted that the axial direction is not shown on Figure 6(b) and Figure 6(d), because the axial direction is pointing perpendicular to the plane of the 2D figures. Such changes in orientations were not needed for the pouch electrode stacks because the layers were oriented in the planes of the elements of the solid elements.

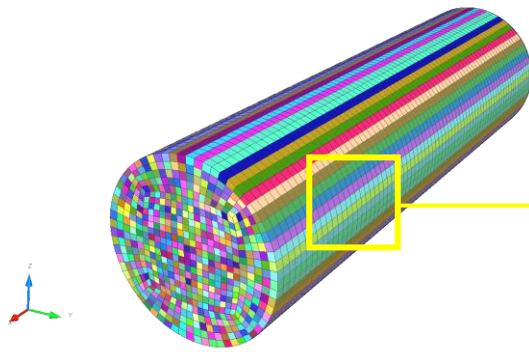
The next section presents the results of the models for all cells simulated using RADIOSS commercial software. Since the jellyroll failure model used was updated to Sahraei failure criterion, no change of the cell model input decks was needed between different loading scenarios. The only changes between different models were the indenter and supporting plates or rods. The average simulation time for each model was about 2.5 hours on a local workstation with 20 CPUs.



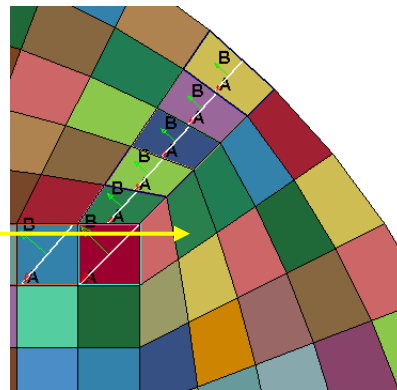
(a) Jellyroll before aligned in LS-DYNA



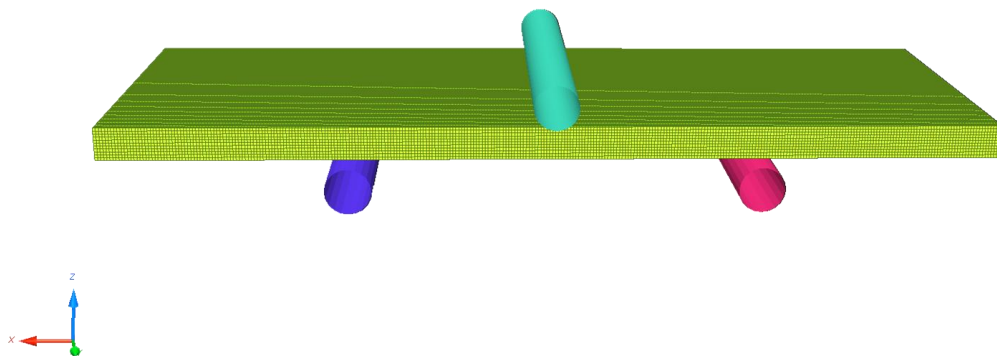
(b) Elements before aligned. A: tangential; B: radial; C: axial (



(c) Jellyroll after aligned in RADIOSS



(d) Element after aligned. A: radial; B: tangential; C: axial.



(e) Pouch cell model under three-point bending set up

Figure 6 Finite element model of the jellyroll with element orientation

CHAPTER 4

VALIDATION OF THE STRUCTURAL ONLY MODEL

4.1 Introduction

This section will show all the comparisons between experimental data and FEM simulation results, including 2 different cylindrical cells and 1 pouch cell. The Sahraei failure criterion will also be compared for the cases have material failure in experiments. Further discussion and conclusions will also be provided in this section.

4.2 Comparison between simulation and experiment

Here the results of simulations for the cylindrical cells and pouch cell studied are presented and compared to experimental data. For the two 18650 cell models, five loading scenarios were simulated, including global compression between two plates in radial and axial directions, local indentations with hemispherical and rod indenters as well as three-point bending. Both cell models had a good prediction of force-displacement behavior, onset of failure and deformation mode. It should be noted that the universal failure criteria, /FAIL/SAHRAEI, was used and all loading cases had the same input file for the cell model with only changing the punch type and load direction. The pouch cell was simulated under six loading cases, including two different hemispherical indentations, one plane-strain rod indentation, a flat through-thickness loading case, an in-plane compression and a three-point bending scenario. The R squares for all simulation versus physical experiment results can be seen in Table 5.

The through-thickness flat compression tests were dominated by global compressive loadings, corresponding to higher compressive to tensile ratios (c_i values), which per Fail

Sahraei criterion should result in the smallest failure strains (ϵ_{fi}). For the cylindrical cell A, the jellyroll failed at strain ratio $c_3=3.93$ with a failure strain of $\epsilon_{f3} =0.09$, see. For cell B the jellyroll failed at strain ratio $c_3=18.92$ with a failure strain $\epsilon_{f3} =0.02$, see Figure 7 and Figure 8 For pouch cell, the compressing plate was a round flat plate, still the strain ratio for this load was dominated by global compression, see Figure 9. The jellyroll failed at strain ratio $c_3=4.2$ with a failure strain $\epsilon_{f3} =0.07$.

The axial/in-plane compressions for neither of the cells lead to fracture of the jellyroll in the experiments. The simulations predicted the absence of failure for such cases for all three cells. For cell A, the test data was shifted with 2 mm based on the unevenness of surface in the physical test, as mentioned in section 2. The first peaks in the experimental data of cylindrical cells were due to the buckling of the shell casings, which the models predicted correctly. After the buckling happened, force began to drop, and the jellyroll strength then became the dominating factor. However, as the largest dimension of the cell was in axial direction, the strains in the jellyroll remained small even at the conclusion of the experiments. This prevented an internal short circuit and failure in the jellyroll from developing in such cases. It should be noted that these loading cases can still lead to short circuits in the end cap or tabs of the cell; however, this type of external short circuit was not the topic of the current study.

Hemispherical and rod indentation load cases included more localized deformations, with both tensile and compressive components. Deformations were concentrated under the contact area between the indenter and the cell. The strain ratios for these cases were higher than the strain ratios of flat compressions, and the failure strain is correspondingly smaller. For cell A under rod indentation, the jellyroll failed at the strain ratio $c_3=0.9913$ with a

failure strain $\epsilon_{f3} = 0.37$; for hemispherical indentation it failed at strain ratio $c_3 = 3.05$ with a failure strain $\epsilon_{f3} = 0.105$. as for cell B, under rod indentation the jellyroll failed at strain ratio $c_3 = 2.483$ with a failure strain $\epsilon_{f3} = 0.125$; and it failed at strain ratio $c_3 = 3.04$ with a failure strain $\epsilon_{f3} = 0.11$ for hemispherical indentation, see Figure 7 and Figure 8. For the pouch cell, it had one rod indentation and two different hemispherical indentations. The rod indentation had a strain ratio $c_3 = 0.9306$ with a failure strain $\epsilon_{f3} = 0.215$; the small/medium hemispherical indentations, both had a strain ratio $c_3 = 0.717/0.653$, and both had failure strains $\epsilon_{f3} = 0.2$, see Figure 9. From the cylindrical cell simulation results, rod indentation had more compression strain dominating which has a smaller strain ratio; hemispherical indentation had more tension loading and a higher strain ratio. Similar trends were observed for both cells A and B. For the pouch cell, all rod and hemispherical indentations had very close strain ratio and failure strain values.

The three-point bending case creates areas of both in-plane tension and in-plane compression combined with through-thickness compression. The shell casing models of cylindrical cells already capture different behavior under tension and compression by the implemented the Modified Mohr Columb failure criteria ⁴³. Looking at the bottom part, where the failure of the jellyroll happened, the elements in that part were more controlled by tension. Thus, the strain ratio was much smaller than any other cases and the failure strain was higher. For cell A, jellyroll failed at strain ratio $c_3 = 0.136$ with a failure strain $\epsilon_{f3} = 0.77$, see Figure 7; for cell B, jellyroll failed at strain ratio $c_3 = 1.275$ with a failure strain $\epsilon_{f3} = 0.15$, see Figure 8. The in-plane and three-point bending for the pouch cell didn't have jellyroll failure. The force drop was due to the formation of a hinge under the punch rather than rupture of layers.

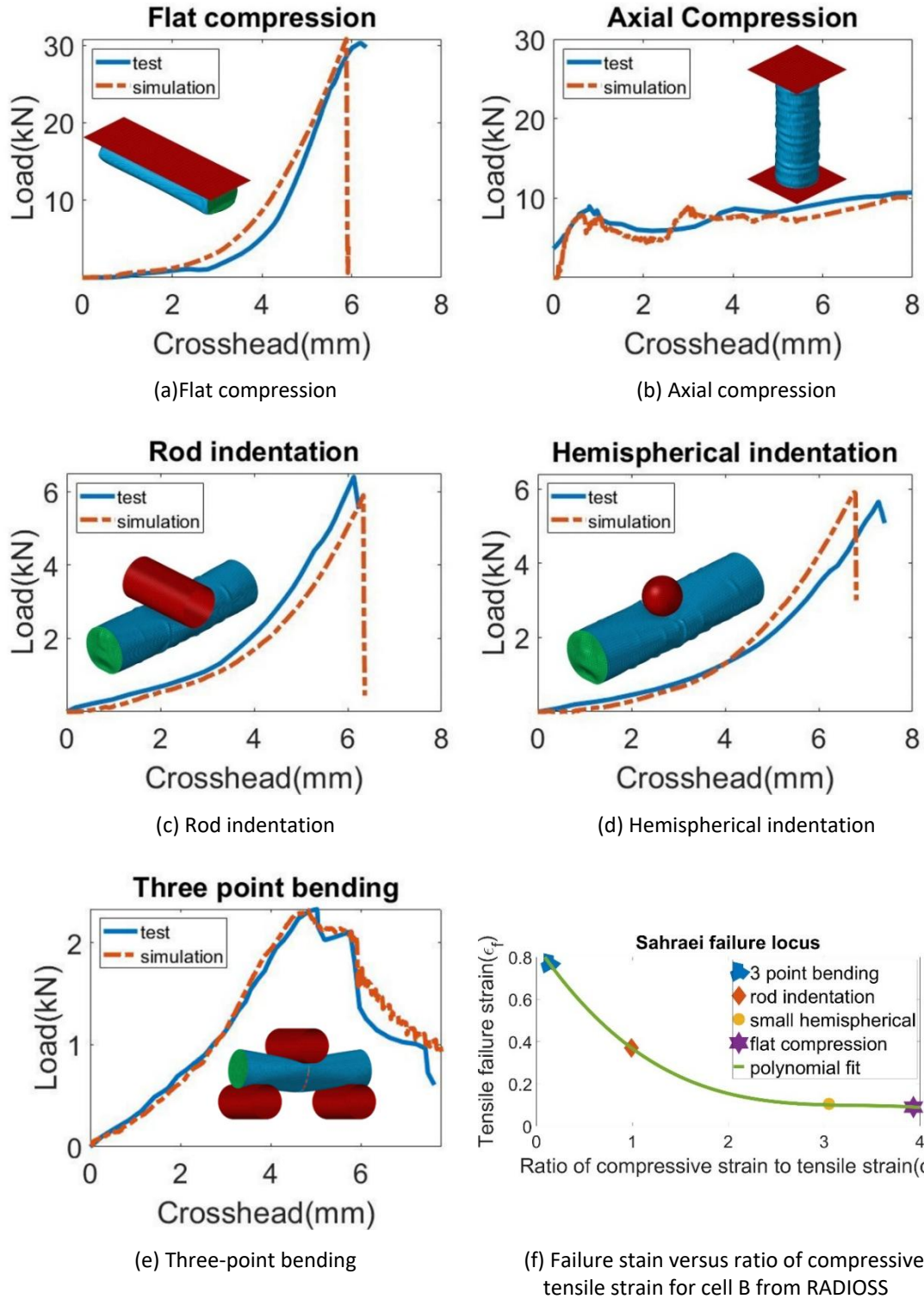
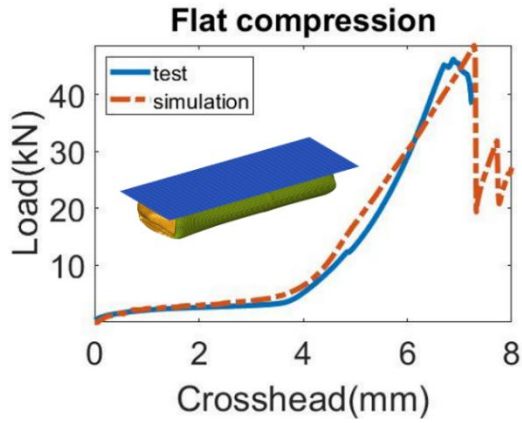
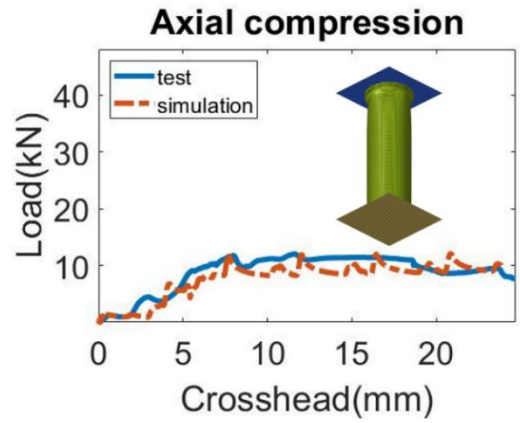


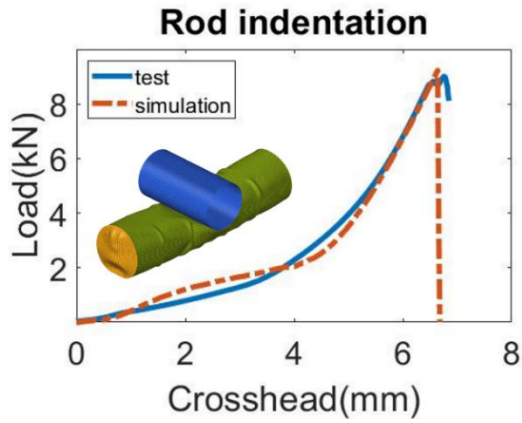
Figure 7 Simulation results of cell A



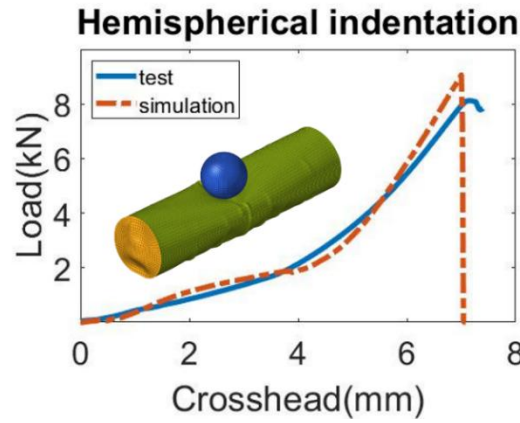
(a) Flat compression



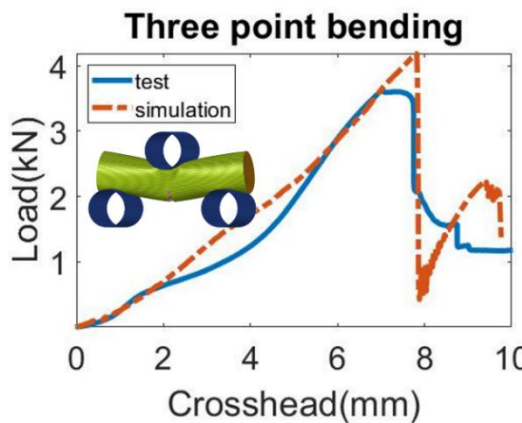
(b) Hemispherical indentation



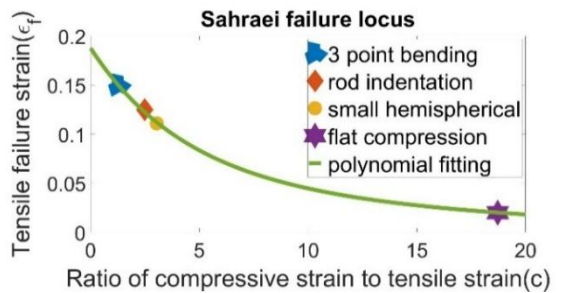
(c) Rod indentation



(d) Three-point bending

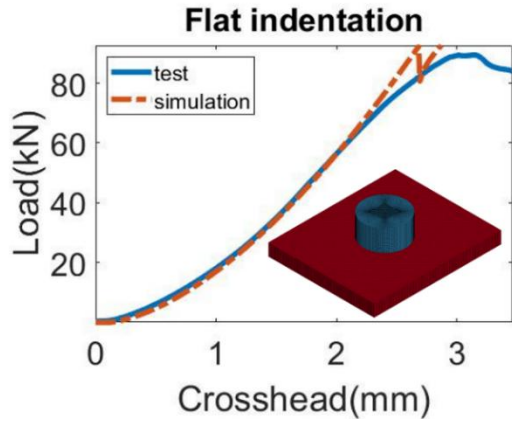


(e) Axial compression

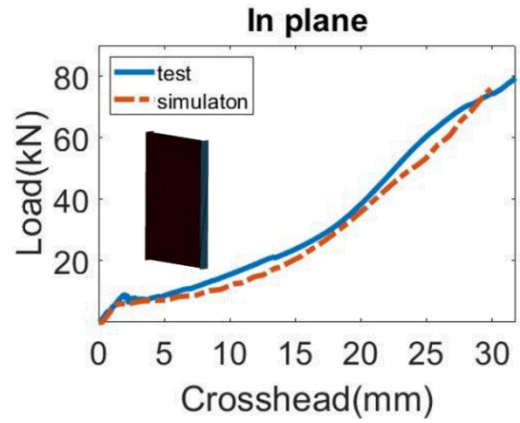


(f) Failure stain versus ratio of compressive to tensile strain for cell B from RADIOSS

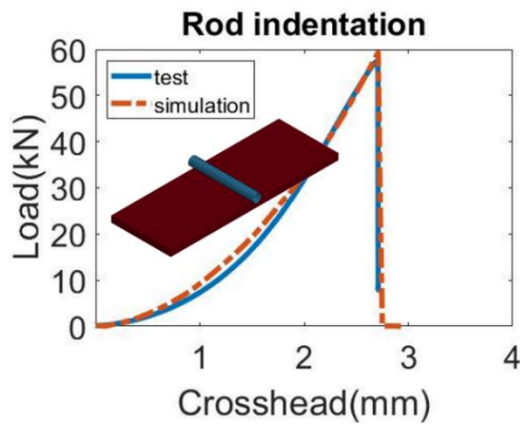
Figure 8 Simulation results of cell B



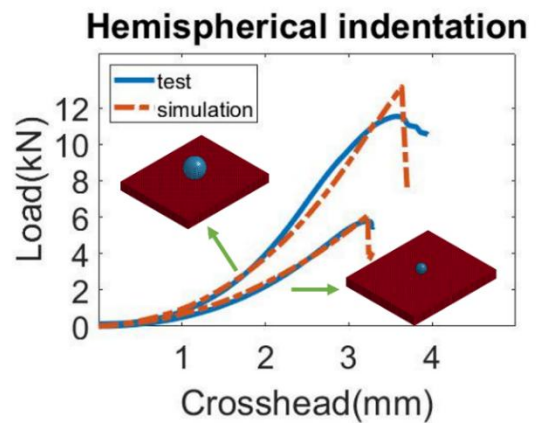
(a) Flat compression



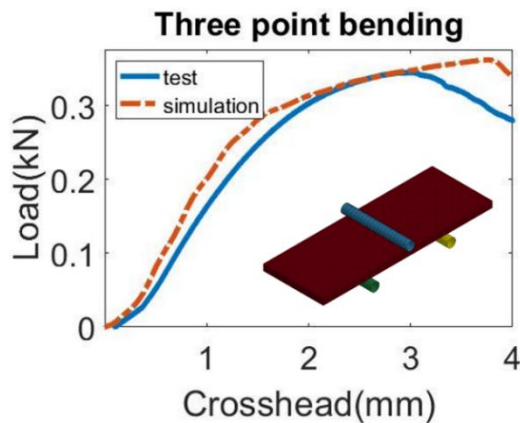
(b) In-plane compression test



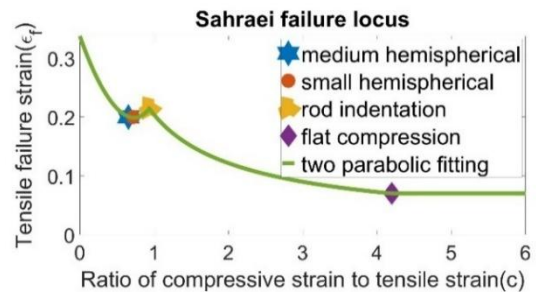
(c) Rod indentation



(d) Small/Medium Hemispherical indentation



(e) Three-point bending



(f) Failure stain versus ratio of compressive to tensile strain for pouch cell from RADIOSS.

Figure 9 Simulation results of pouch cell

Table 5 R square for all simulations

Cell A	R Square	Cell B	R Square	Pouch cell	R Square
3pb	0.9759	3pb	0.906	3PB	0.9625
Flat	0.9791	Flat	0.981063	Flat	0.9973
Hemi	0.9894	Hemi	0.984	S Hemi	0.9946
Rod	0.999	Rod	0.9867	Rod	0.9963
Axial	0.84	Axial	0.8966	M Hemi	0.99452
				In-plane	0.9948

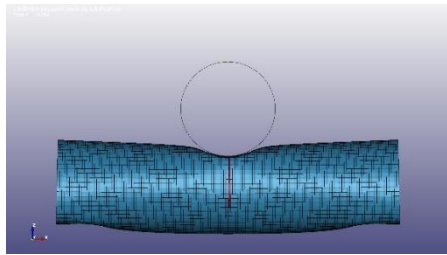
4.3 Discussion

4.3.1 Comparison of the failure criteria and anisotropy of casing material

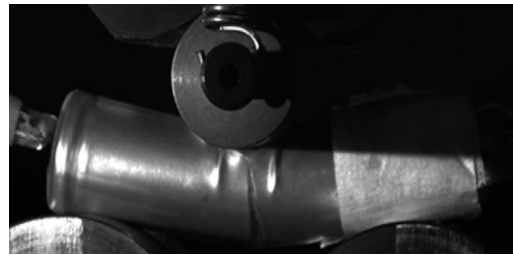
A simple failure criterion may be enough when dealing with simple loading, but it cannot predict the failure correctly when the loading becomes complex. See Figure 10(a). The simulation used constant failure strain for three-point bending. Since the deformation happened on the middle top of the casing first, the strain value in that area will accumulate first. Elements will then be deleted if the strain value reaches the criteria. For such failure criteria, failure will always be obtained on the top of the battery casing, which does not follow the casing behavior in the test: from Figure 10(b), we see cracks first obtained from the bottom of the cell.

The solution to this issue is MMC. This failure criterion provides different plastic strains for tension and compression. In compression, the failure strain is quite large, which is the deformation happening on the top middle of the bottom; In tension, the failure strain is small, which is the bottom part deformation. In this way, the bottom part of the casing will be easier to fail, while the top part of the casing element will stay, see Figure 10(c).

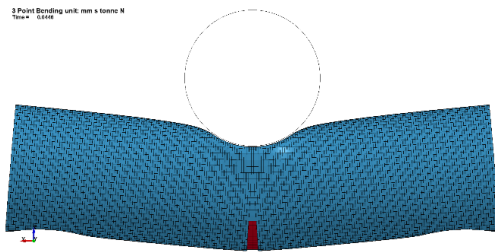
Anisotropic model for shell casing provides different properties for different directions. For three-point bending, the result is very similar until 4 mm displacement, see Figure 10(d), isotropic shell casing has a peak force for casing failure at 4.5 mm displacement, whereas the anisotropic shell casing has the failure at 6 mm displacement, see Figure 10(d).



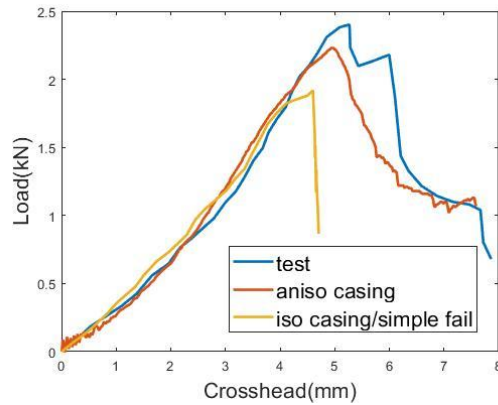
(a) Crack for three-point bending using maximum strain failure criterion



(b) Crack from the test



(c) Crack for three-point bending using MMC failure criterion



(d) Force-displacement result for three-point bending comparison between anisotropic casing material with MMC failure option and isotropic casing with simple failure criteria

Figure 10 Comparison between different failure criteria

4.3.2 Comparison of the anisotropy of jellyroll material

The axial compression shows the main difference between the isotropic and anisotropic material models, see Figure 11. All the other simulation cases are dominantly controlled by the compressive properties in the lateral direction and/or by the tensile strength of the layers. The properties of the isotropic crushable foam model have been fully calibrated for

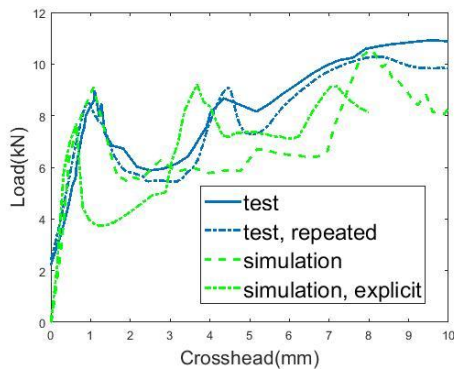
lateral loading cases, which does not take into account the additional strength from metallic layers present under in-plane/axial loadings. The anisotropic material of honeycomb allows calibration of this increased compressive strength in axial direction, which makes it superior in prediction of load-displacement under this type of loading.



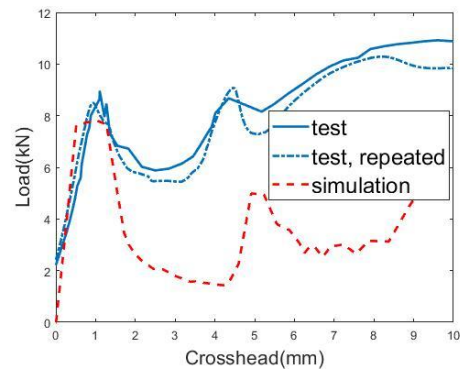
(a) Simulation deformation model



(b) Test deformation mode



(c) Force-displacement result for honeycomb material, first simulation is implicit-explicit, second simulation with 'explicit' legend is explicit only



(d) Force-displacement result for crushable foam material

Figure 11 Comparison between anisotropic and isotropic material for axial compression

During axial compression, a buckling of shell casing happens. Therefore, the implicit-explicit solver has been chosen to get the buckling peak force more accurately in this load case. By using the implicit solver at the beginning of the analysis, a more accurate

prediction of the critical buckling load is achieved. The simulation then switches to explicit analysis to allow the solution of large displacements under dynamic loading. If only an explicit analysis is performed, the accuracy of the prediction in the initial part of the deformation slightly decreases, as the initiation of buckling will be controlled by the numerical errors that come from explicit solver rather than the eigenvalues calculated from the buckling analysis. This explicit only simulation is added for the case of the honeycomb model for comparison.

The first peak in the curves corresponds to the buckling strength of the shell casing. The implicit/explicit models with both honeycomb and isotropic crushable foam predict this peak value closely, as it does not heavily depend on the jellyroll properties. However, right after this peak value, the jellyroll strength becomes important. The isotropic model, which does not take into account the additional strength from the foils under in-plane loads, shows a much lower force value compared to experiments in displacements beyond the first peak force. The anisotropic honeycomb model shows its superior capabilities in predicting the cell response under this loading scenario, as this model predicts the higher-level strength of the cell after the first peak in the load. This is because the contribution of the foils' buckling strength is added to the stress-strain input of the material model in this direction. It should be noted that the first 2 mm of deformation in these experiments is where the contact between the cell's top and bottom surfaces and the punch are being built. The details of the non-even surface of the jellyroll/casing are not included in these homogenized models. Therefore, that delay in the engagement between the punch and the cell is not simulated by the model. It should be noted that axial loading is a very important case for batteries in EVs such as Tesla, where the cells are located under the passenger

compartment in the vertical direction, and a ground impact moves such cells into axial loading right away, which may cause failure and short circuit in the cells or battery packs leading to thermal runaway and fire³¹.

4.3.3 Comparison of failure curve

We applied Sahraei failure criteria to two cylindrical cells and one pouch cell to predict short circuit under various types of indentation using homogenized models. All simulations show good prediction of the force-displacement behavior and force drop and element erosion at the onset of internal failure. The failure loci of 3 different cell models studied here and the original curve data obtained from RVE model⁵⁰ are plotted in Figure 12. The common trend of these curves is having large failure strain (ϵ_f) value when the strain ratio (c) is low and having small failure strain (ϵ_f) value when strain ratio (c) is high.

Cell A had a significantly higher failure strain (ϵ_f) value compared to all others in low strain ratio region where the three-point bending case falls, and a narrower range of the strain ratios, c between 0 to 4. As this cell is not available anymore for investigation of micro components, it is not clear what the source of such specific properties are. However, it should be noted that this cell was a very early generation of the 18650 cylindrical cells acquired in 2010 and with lithium cobalt chemistry. The range of strain ratios (c) of cell B were from 0 to 18, which is also similar to what we found in Sahraei's 2016 work. For the pouch cell, the shape of the failure locus looks like a combination of two parabolic curves. In Figure 9(f), the hemispherical and rod indentations had very close strain ratios. Considering the size of the pouch cell, these deformations are more localized in the center area and not affecting the whole cell. The similarity of strain ratios for different size

hemispherical punch loads explains how earlier literature reported one single value of failure strain could predict all kinds of local hemispherical indentations, see Sahraei's 2012 and 2014 work^{15,51}.

This failure model also worked for loading cases which didn't have failure. In those cases, like axial compression for cylindrical cells and in-plane compression for pouch cell, elements were compressed and had high values of strain ratio, however the global deformation generated a uniform deformation, thus the strains did not get localized and did not reach the failure criteria. In the cases of the three-point bending loads, the strain ratio (c) was very small, so the cylindrical cells had their largest failure strain (ϵ_f) and the pouch cell did not reach a failure strain at all.

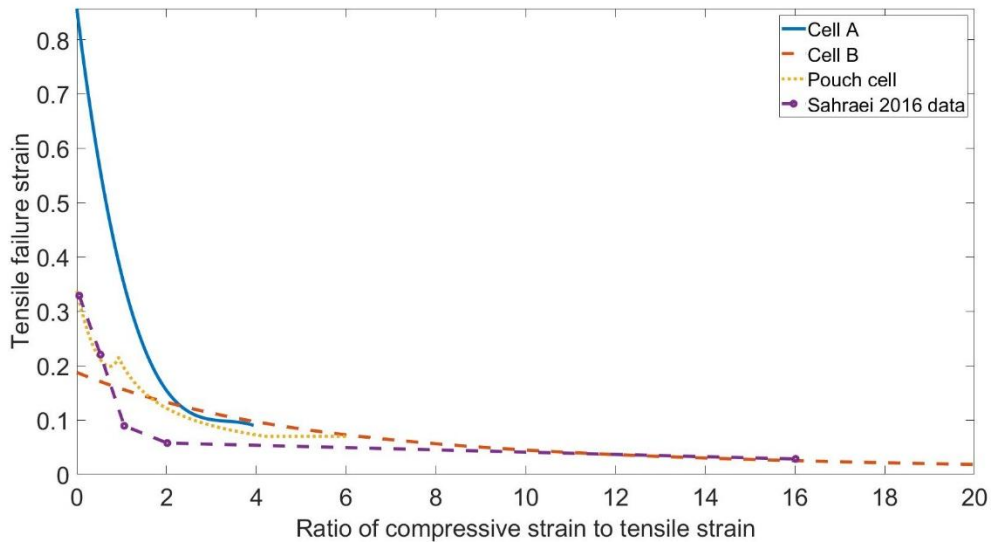


Figure 12 Failure curve comparison for cell A, cell B and pouch cell

CHAPTER 5

ENHANCEMENT OF SAHRAEI FAILURE CRITERIA WITH REAL PHYSIC EFFECTS

5.1 Introduction

Upon to this point, all tests and model simulations mentioned above were conducted with pure discharged cell, at room temperature and under quasi static deformation. According to our previous study, the materials and Sahraei failure model successfully predicted mechanical force-displacement during different loadings. The next step to improve the failure criterion is to add more factors to it. Here we listed four common factors for Li-ion battery cell during deformation: Temperature, strain rate, state of charge (SoC) and aging.

The current failure model with all material property calibrated has been validated with short circuit predictions under room temperature, fully discharged and quasi-static loadings. For future steps, we are trying to add more factors to the Sahraei Failure Criterion. To achieve this goal, experiments for temperature, SoC, strain rate dependency must be accomplished. These tests are designed to isolate the influence of each parameter and capture the coupling effects that may arise between them. Aged cell test data will be extracted from previous literature. The experimental results will guide the reformulation of the governing equations from the original Sahraei failure model, enabling us to introduce correction terms or scaling factors that account for these physical dependencies.

For model validation after experiments, we can use the same procedure in sections 3 and 4. The overall objective for this section is to develop an advanced failure criterion

which can predict battery mechanical behavior under different temperature and different velocity of the impact.

5.2 Method

5.2.1 Battery specification

The Li-ion battery cell used in this research of real physic effect is a lithium-iron-phosphate 18650 cylindrical battery. The nominal Capacity is 1.5 Ah and nominal voltage is 3.2 V.

5.2.2 Test method

For study of the temperature effects, indentation tests were performed using a steel rod with a diameter of 15.8 mm, tested with different temperatures from -40 °C to 60 °C. A thermal chamber was used to ensure the temperature at testing. Since the deformation primarily occurs at the center of the cell, the terminals remain unaffected under this type of loading. An internal short circuit can be identified by a simultaneous drop in voltage and force. A thermal chamber was used to maintain different temperatures during the test. An INSTRON 8341 multimeter was used to measure voltage, with two wires taped to the battery terminals⁶¹. Cells are fully discharged for this test.

In this test, we can see with the increase of temperature, the peak force and displacement at failure also increased, in a range of 6.3 mm to 7.7 mm and 7 kN to 11.7kN, shown in Figure 13. Among all 6 tests, only tests at 20 °C and 0 °C have a very similar peak force, and 20 °C test's peak force is a little higher than the 0 °C test, but the general trend for this series of test is that with higher temperature, the peak force at failure is lower.

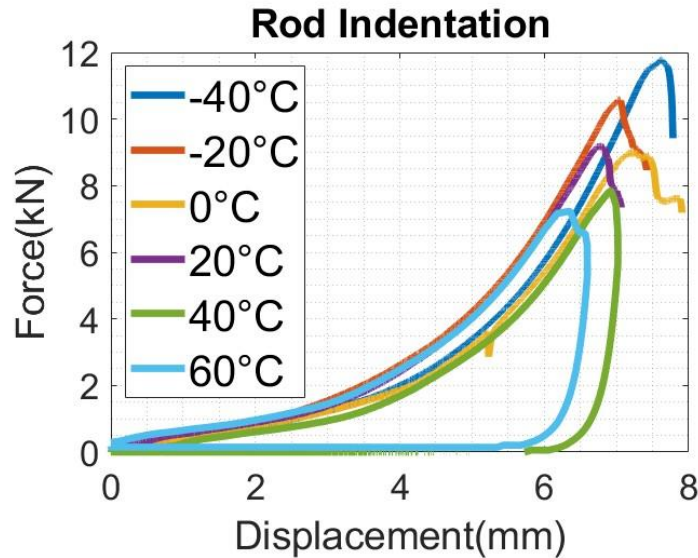
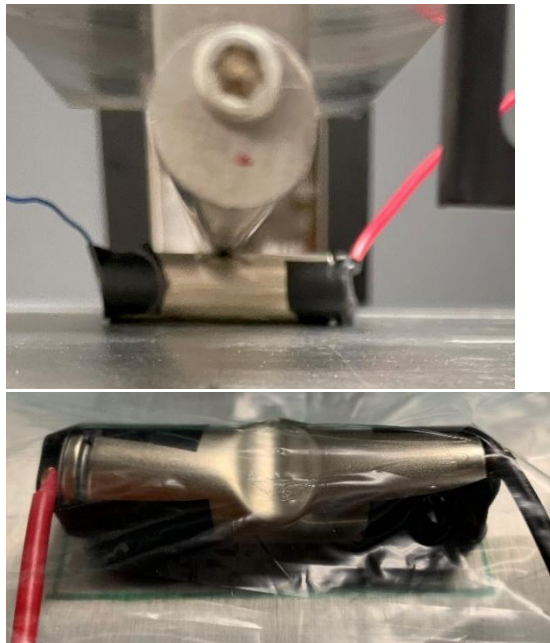


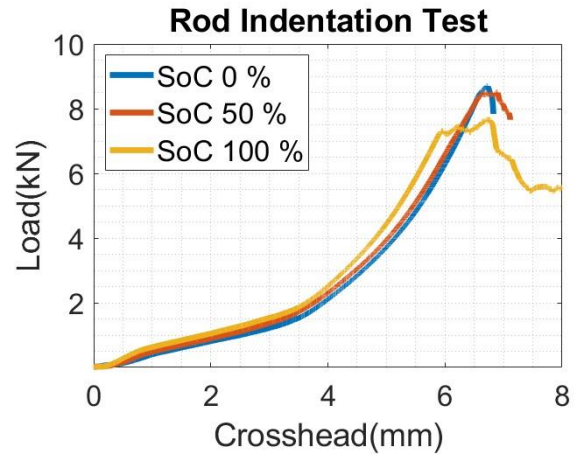
Figure 13 Rod indentation at different temperatures

For the SoC study, the same experimental setup used in the temperature-dependent compression tests was employed for this investigation, ensuring consistency across test conditions. Cylindrical rod intrusion tests were performed on cells at three distinct states of charge (SoC): 0%, 50%, and 100%. A steel rod with a diameter of 15.8 mm was driven vertically into the center of each cell at a constant rate of 1 mm/s. Prior to testing, cells were carefully charged or discharged to achieve the targeted SoC levels, with voltage verification to ensure accuracy.

The results clearly demonstrate that the state of charge significantly influences both the mechanical response and failure characteristics of the cells. See in Figure 14, as SoC increases, not only the peak force at failure decreases, but the stiffness of the cell structure also increases, indicating a change in material behavior likely driven by internal pressure and structural expansion of the jellyroll due to lithium intercalation.



(a) Test set up and deformed cell after test



(b) Test result with 0%, 50% and 100% SoC

Figure 14 Rod indentation under different SoC

At 0% SoC, the cell exhibited a peak failure force of 8.7 kN at a displacement of 6.7 mm, reflecting relatively ductile behavior. In contrast, the 100% SoC cell displayed a stiffer load-displacement curve and failed earlier, with a lower peak force of 7.26 kN occurring at just 5.9 mm displacement. This suggests that cells at higher SoC levels are more susceptible to brittle-like failure under mechanical intrusion, likely due to increased internal stresses and reduced energy absorption capacity. The 50% SoC results fell between the two extremes, further supporting the correlation between SoC and mechanical performance.

In order to test battery's behavior under different strain rates, dynamic rod impact tests were performed on Gravity Impact Tester for Battery Testing (UN 38.3.4.6 & IEC 62133)-MSK-TE902-UL, see in Figure 15(a). This machine has a 10 kg mass block on top, the initial velocity at contact can be determined by the initial height of the mass block. The cell was placed on the supporting plate with L shape brackets to align with the rod indenter

attached to the bottom of the block. Voltage measurement is not available in this test since the contact duration is less than 8 milliseconds, the voltage measurement tool was not capable of getting enough data points.

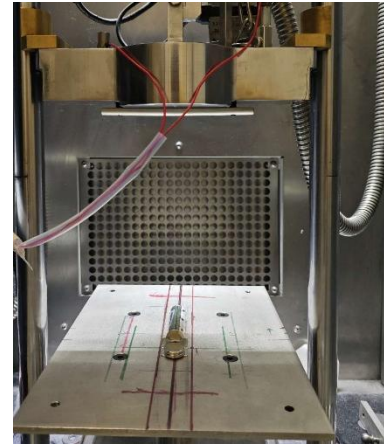
When the experiment starts, the weight at a certain height will be released, and the mass block will then have a free drop motion until the rod indenter hits the battery cell. During the whole test, force is measured by the load cell underneath, acceleration is measured by the 2 accelerators on the block and then converted to displacement in millimeters.

In this research, 3 m/s velocity at contact have been conducted. Cells are fully discharged to ensure the safety of the experiment.

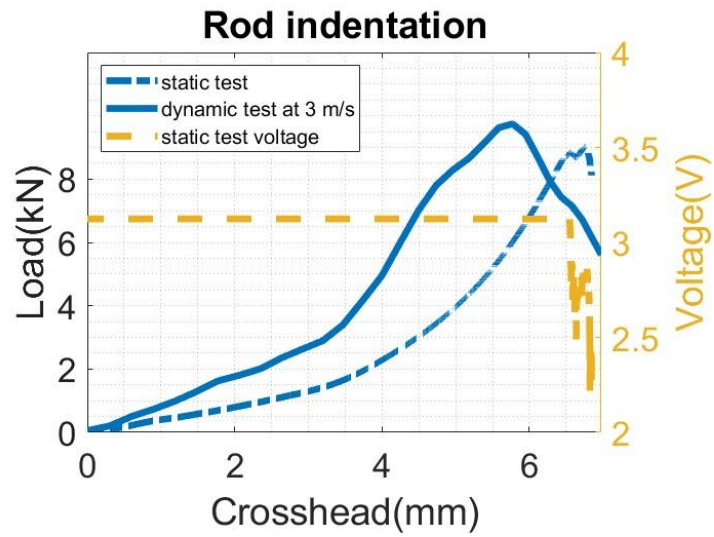
From the data shown in Figure 15(c), we can see under high-speed impact test, the cell showed a stiffer behavior, the peak force for test at 3 m/s and 0.0167 m/s are 9.74 kN and 8.78 kN, however the displacement at peak force for those two tests are 5.77 mm and 6.53 mm.



(a) MSK-TE902 machine



(b) Test set up with cell.



(c) Test result for both dynamic and static under rod indentation

Figure 15 Dynamic rod impact test

5.3 Finite element modeling

In this section, we will discuss the development of the jellyroll material model with SoC expansion and strain rate dependence. We will also discuss the development of modeling the Sahraei failure criteria with temperature, SoC and strain rate effect.

5.3.1 Material modeling

The jellyroll model used honeycomb material in RADIOSS from our previous work, in this work, we will add more features to the existing honeycomb material card and make it more similar to battery jellyroll material⁹⁶. This new material will have the expansion behavior due to SoC difference and strain rate dependence.

The jellyroll of the cylindrical cell will expand during charging and discharging⁹⁷. This procedure will generate pre-stress even before external loading happens. To capture the same behavior, a volume expansion feature must be added to the current material card. From Mehdi's paper about SoC and jellyroll expansion, 3% volume expansion was found at 100% SoC of the 18650 Li-ion battery's jellyroll used in this work. To achieve this function, before the deformation happened, we let the SoC grow from 0%. At the same time, the element will be expanding, once the SoC reached the desired value, expansion will stop, and the deformation then will start. Further detail about the expansion calibration can be found in Mehdi,2024⁹⁸.

As observed in dynamic and static testing, cells usually behave stiffer under high strain rate tests. To capture this behavior, we introduced strain rate dependent stress-strain curve of the jellyroll as the strain rate effect, which makes it possible to have different material stiffness between different tests with different speed.

5.3.2 Failure criteria enhancement

The cell model and Sahraei failure criterion have been developed in author's previous works^{43,99}. Modeling work in this research is coupling different features to model and failure criterion. Temperature and SoC coupling were validated on RADIOSS, the dynamic loading was validated on LS-DYNA.

Temperature, strain rate, SoC and aging effect can be edited to the failure card /FAIL/SAHRAEI, where we add temperature, SoC, strain rate and aging as another factor counting into the failure strain calculation.

The governing equation of the coupled failure model is shown below:

$$\begin{aligned} \varepsilon_f(c, T, n, SoC, \dot{\varepsilon}) = & \varepsilon(c) * \left(1 - \left(\frac{T - T_r}{T_m - T_r} \right)^n \right) * (1 - c_{SoC} * SoC) * \\ & \left(1 - c_\varepsilon \ln \frac{\dot{\varepsilon}}{\dot{\varepsilon}_{st}} \right) * (1 - c_{cycle} * cycle) \end{aligned} \quad (15)$$

The mechanical behavior of lithium-ion battery cells under multi-physics conditions was investigated through three independent variables: temperature, state of charge (SoC), strain rate and aging. To comprehensively evaluate their individual effects, each parameter was isolated within controlled experimental domains. The temperature range spanned from -40 °C to 60 °C, encompassing extreme operational limits for electric vehicles in arctic and tropical climates. SoC levels were validated at three critical thresholds: 0% (fully discharged), 50% (nominal operating point), and 100% (maximum energy storage capacity). Strain rate sensitivity was examined through dynamic rod indentation tests at 1 mm/min (quasi-static regime) and 3000 mm/min (high-rate dynamic loading), representing scenarios from gradual mechanical abuse to catastrophic crash events. To investigate the

aging effect, we benchmarked our model's predictive capability against previously published studies, focusing on its ability to capture mechanical degradation over cycling. This comparison ensures that the model accurately reflects early failure mechanisms driven by electrochemical-mechanical coupling. Specifically, the model is validated across a cycling range from 0 (fresh cell) to 1200 cycles, demonstrating its robustness in predicting the progressive loss of structural integrity and potential onset of mechanical failure commonly observed in aged Li-ion cells.

Table 6 Nomenclature in the equation

nomenclature			
ε_f	Strain at failure	SoC	Current SoC
c	Strain ratio	c_ε	Strain rate coefficient
T	Current temperature	$\dot{\varepsilon}$	Current strain rate
T_r	Room temperature	$\dot{\varepsilon}_{st}$	Strain rate for static test
T_m	Reference temperature	c_{cycle}	Aging coefficient
n	Temperature exponent	cycle	Cycle number
c_{SoC}	SoC coefficient		

The fundamental FEM model of this research was introduced in Song's 2024⁹⁹. This model of cylindrical cell had 2 components, a metal shell casing and jellyroll. The model was validated with Sahraei failure model under room temperature, 0% SoC and quasi-static conditions. In this work, we will validate the model under different temperatures, SoCs and strain rates conditions mentioned in the previous paragraph. For the strain rate study, we provided a strain rate dependent honeycomb material¹⁰⁰.

5.4 Model validation

In this section, we will compare all model simulation results to the experiments mentioned in section 5.1 and provide the validation of the enhanced failure criteria.

5.4.1 Failure validation of rod test under different temperature

As described in Section 2, rod indentation tests were conducted on cells across a temperature range from -60°C to 40°C to evaluate temperature-dependent mechanical behavior. The results reveal a clear trend: as the temperature increases, the peak force at failure also rises, increasing from 7.22 kN at 40°C to 11.76 kN at -60°C . This behavior reflects the temperature sensitivity of the cell materials.

For the purpose of finite element model (FEM) validation, simulations were performed using a baseline (room) temperature of T_r , a melting temperature of T_m , and a temperature exponent n , as prescribed in the thermal function. To isolate the temperature effect, the influence of state of charge (SoC), strain rate and aging were intentionally suppressed by setting c_{SoC} , c_{ϵ} and c_{cycle} in Equation 15. This allows for a focused comparison between experimental and simulation data under varying thermal conditions.

The simulation results show strong agreement with the experimental data, particularly in predicting the peak failure force. Notably, as temperature decreases, the model also captures an increase in failure strain, which manifests as a delayed onset of the force drop during rod indentation. The failure strain for each case is differently calculated with

Equation 15, reflecting a decreasing peak force with the rise of temperature.

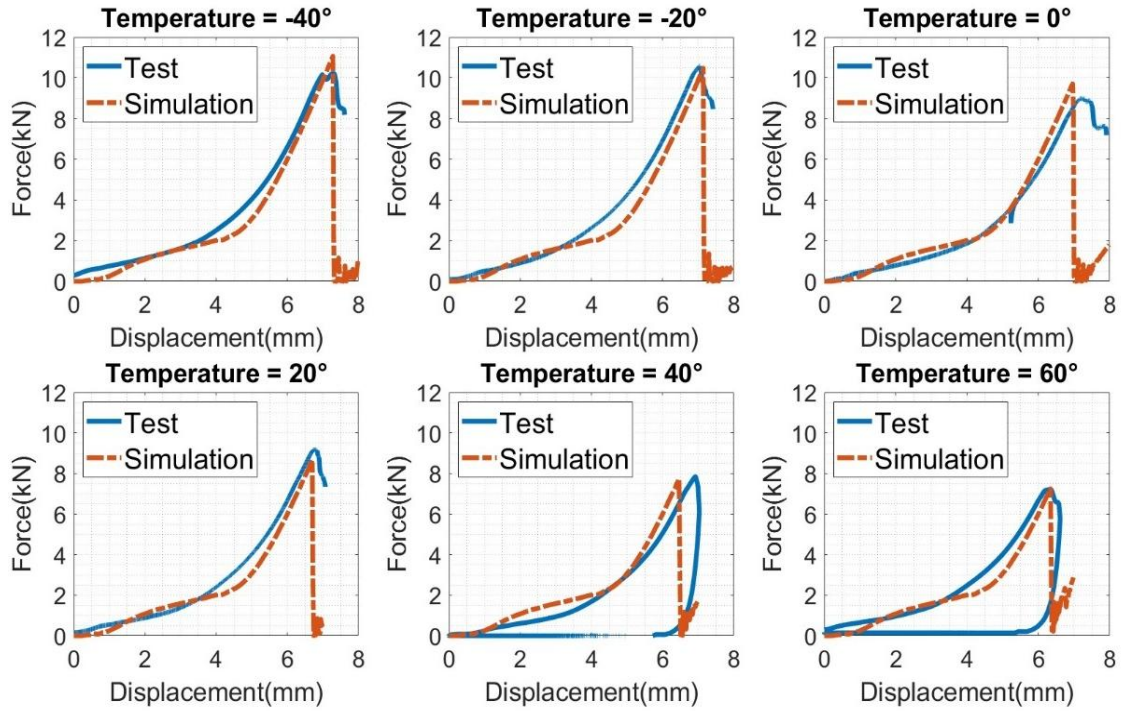


Figure 16 Model validation for different temperature rod indentation test.

5.4.2 Failure validation of rod test under different SoC

Building upon the findings of Mehdi 2024’s work, two key differences in mechanical response under rod indentation are observed across cells with varying states of charge (SoC). First, the peak force at failure decreases as the SoC increases. To accurately capture this behavior in the simulation model, a SoC sensitivity coefficient c_{SoC} was implemented in Equation 15, allowing the failure strain to vary proportionally with the SoC level. It is important to note that within the model, SoC is represented as a normalized input, where 0 corresponds to 0% SoC and 100 represents 100% SoC.

The second major difference is related to material stiffness. Due to electrochemical swelling and internal pressure buildup, cells at non-zero SoC levels exhibit increased

stiffness. This effect becomes more pronounced as SoC rises, reflecting the progressive expansion of the jellyroll structure. To account for this behavior, volumetric expansion was incorporated into the jellyroll material model. This addition enables the simulation to not only reflect the structural stiffening but also capture the strain hardening behavior associated with elevated SoC conditions.

For this SoC-focused validation, the effects of temperature strain rate and aging were intentionally deactivated by setting the room temperature and current temperature equal $T_r = T$ and the strain rate sensitivity coefficient, aging coefficient $c_\epsilon = c_{cycle} = 0$ in Equation 15. This isolates the influence of SoC on failure behavior, ensuring a clearer interpretation of SoC-induced mechanical variation.

In the validation we can see highly matched simulation result as compared to the test data, both peak force, displacement at failure, and material stiffness matched well.

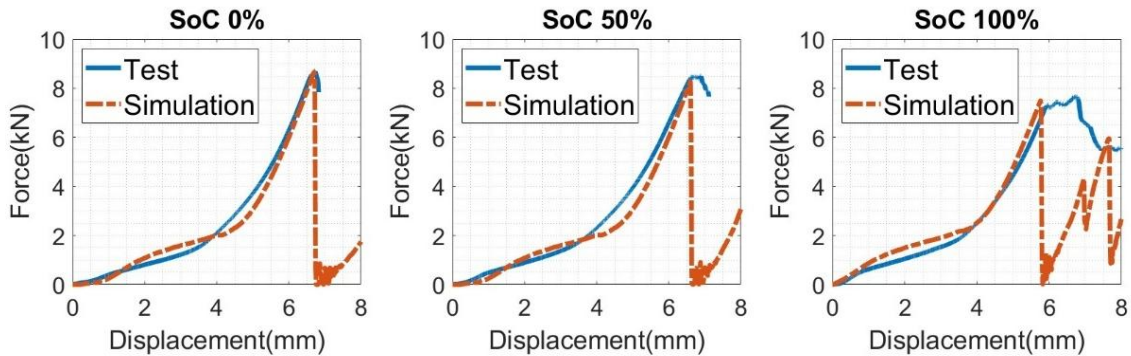


Figure 17 Model validation for different SoC rod indentation test.

5.4.3 Failure validation of rod test under different strain rate

The third validation in this work will be strain rate effect, from section 5.1, we can see battery behaved stiffer during high-speed impact test, at 3000mm/s. By taking account of the strain rate effect in Equation 15, we are able to get different material responses under different testing velocities.

The failure is also validated in this model under different strain rates. While looking at two test data, we can see the dynamic test has higher peak force at failure, however since material gets stiffer, the failure strain is smaller, here we use c_ε in Equation 15 to control the model has correct failure point, as same as all other model validation, temperature, SoC and aging consideration is not active. For the dynamic impact model validation, a peak force at 9.78 kN at 5.45 mm which is very close to the experiment.

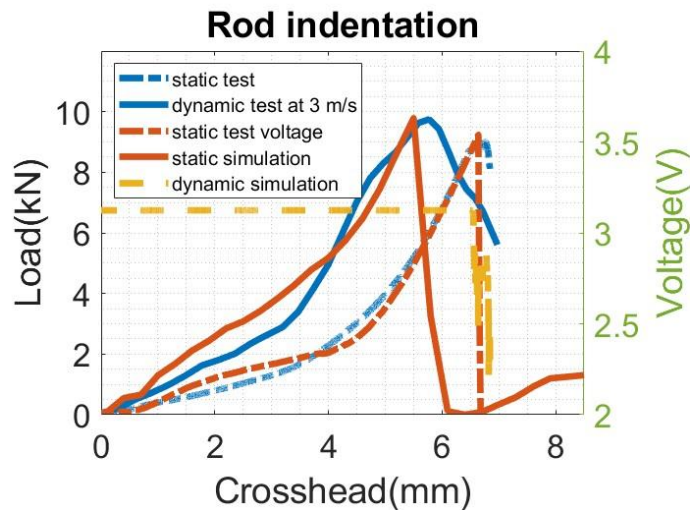


Figure 18 Comparison between dynamic and static rod test

5.4.4 Model capability for aged cell prediction

Final validation with the enriched Sahraei failure criteria is the aging effect. Different from other validations, due to the lack of experimental results, we are validating our failure

criteria with previous literature results. In Zhang et al 2017, an elliptical cell was indented with 0 cycle (fresh cell) and 1200 cycles. The material stiffness shows very similar result; however the fresh cell has a peak force at failure 4.7kN and the cycled cell has a peak force at failure 4.3 kN³. In our model, we use the cylindrical cell model to validate the ability of aging effect prediction. The fresh cell at 0 cycle has a peak force at 9.2 kN and the 1200 cycle cell has a peak force at 8.19 kN, which is very close to the ratio compared with the elliptical cell in the literature, see in Table 7.

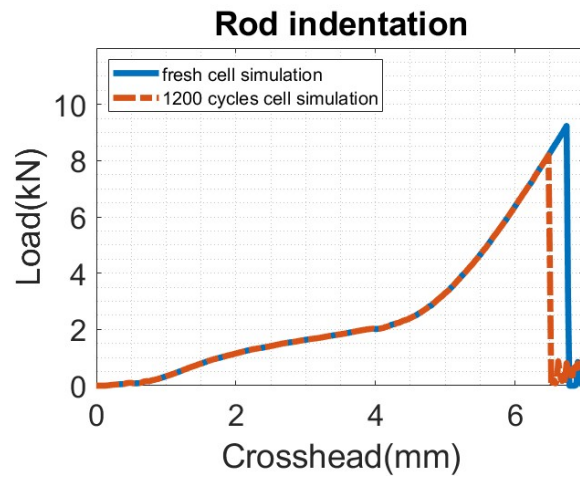
Table 7 Aging effect comparison with literature

	Literature elliptical cell	K2 cylindrical model
Peak force at failure for 0 cycle cell	4.7 kN	9.2 kN
Peak force at failure for 1200 cycle cell	4.3 kN	8.19 kN
Peak force difference	10%	10%

Again, to isolate the aging effect only, room temperature and current temperature should be same to deactivate temperature effect, c_{SOC} , c_{ϵ} are defined 0. The cycle number is 1200 as aligned with the test, and a coefficient c_{cycle} is used.

For future work, we will perform indentation tests for cylindrical cell B, use the Sahraei failure model predicted short circuit in modeling. The fresh cell has been charged with 1.5 A current (1C) and discharged with 3.0 A (2C) between a voltage limit of 4.1V and 2.0 V. Two different stages of aging has been planned: one cell has 315 cycles and the capacity now is 1.04 Ah which is below 75% of the fresh cell's capacity; the other one cell has 580 cycles and the capacity now is 0.30 Ah which is close to 20% of the fresh cell's capacity.

Test data and simulation results will be shown in future publications.



x

CHAPTER 6

CONCLUSION

In this study, a full homogenous FEA model was developed for an 18650 cylindrical Li-ion battery, containing two parts, a shell casing, and a jellyroll inside that. The plastic properties of shell casing were obtained from a window shape specimen test result reported by Zhang and Wierzbicki 2015 and calibrated with a combined Voce-Swift law. MMC failure criteria was then coupled to the casing material ⁴⁴. Two different material models were used for the jellyroll an isotropic crushable foam model and an anisotropic honeycomb model. Extra strength in axial direction was added on the anisotropic honeycomb material for the jellyroll. The two models were then validated with different mechanical loadings, including two plate compression, rod indentation, hemispherical indentation, axial compression and three-point bending. All predictions were very close to the experiments except the isotropic cell model under axial compression loading. The isotropic model was not capable of predicting this loading condition because the additional strength of the jellyroll due to its structural anisotropy and extra strength of metallic foils under in-plane loading was not accounted for in the isotropic model.

Additionally, we calibrated and validated the Sahraei failure model for three different cell models: two cylindrical cells and a pouch cell. The background on this failure model was developed based on simulations of a small elliptical cell RVE in 2016. In the current work, the model was coded in commercial software Altair RADIOSS and the failure loci for the three cells were calibrated and then predictions of internal failure were validated. The loadings included flat and axial compressions, rod and hemispherical indentations and three-point bending for cylindrical cells. For pouch cells, the loadings included flat and in-

plane compressions, rod and two hemispherical indentations and three-point bending. All cell models coupled with failure models had good predictions of the force-displacement and failure behavior, with R squares of about (give average) on average.

By taking the consideration of real physic effect on batteries, we add temperature, SoC, strain rate and aging features to the developed Sahraei failure. We conducted several rod indentation tests under different temperatures, SoC and strain rate conditions. For the aging effect on battery's mechanical response, we find the comparison from literature with fresh and cycled cells. By establishing the governing equation with all the features mentioned above, we enhance our base Sahraei failure criteria with the consideration of real physic conditions. The failure criteria then added to the cell FEM model and then validated with all experimental and literature data, shows highly robust result for all different real physic conditions.

CHAPTER 7

CONTRIBUTIONS

The contribution for Yihan Song is listed (with reference):

1. Sahraei failure coding in RADIOSS software user defined failure model for all three different cells and cell model validations. (Paper ready for publish)
2. Computational modeling of cylindrical cell A⁴³.
3. Sahraei failure model enhancement in RADIOSS user-defined material coding coupled with temperature, SoC, strain rate and aging.

Contributions from others (with reference):

1. Experimental data for cylindrical cell A, RVE model development by Dr. Elham Sahraei^{14,50} (PI for EVSL, Temple University)
2. Experimental data for cylindrical cell B, material calibration and cell testing under different temperature by Dr.Mehdi Gilaki⁴⁶ (former EVSL member).
3. Experimental data and computational modeling for pouch cell by Huzefa Saifee Patanwala (current EVSL member).
4. Software support from Marian Bulla and OPENRADIOSS¹⁰¹.
5. General idea of material and failure calibration of the shell casing from Xiaowei Zhang's work⁴⁴.

REFERENCES

1. Etacheri V, Marom R, Elazari R, Salitra G, Aurbach D. Challenges in the development of advanced Li-ion batteries: A review. *Energy Environ Sci.* 2011;4(9):3243-3262. doi:10.1039/c1ee01598b
2. Kermani G, Sahraei E. Review: Characterization and modeling of the mechanical properties of lithium-ion batteries. *Energies.* 2017;10(11). doi:10.3390/en10111730
3. Zhang X, Zhu J, Sahraei E. Degradation of battery separators under charge-discharge cycles. *RSC Adv.* 2017;7(88):56099-56107. doi:10.1039/c7ra11585g
4. Dunn B, Kamath H, Tarascon JM. Electrical energy storage for the grid: A battery of choices. *Science (80-).* 2011;334(6058):928-935. doi:10.1126/science.1212741
5. Viebahn P, Nitsch J, Fishedick M, et al. Comparison of carbon capture and storage with renewable energy technologies regarding structural, economic, and ecological aspects in Germany. *Int J Greenh Gas Control.* 2007;1(1):121-133. doi:10.1016/S1750-5836(07)00024-2
6. Parra D, Patel MK. Effect of tariffs on the performance and economic benefits of PV-coupled battery systems. *Appl Energy.* 2016;164(2016):175-187. doi:10.1016/j.apenergy.2015.11.037
7. Muenzel V, Hollenkamp AF, Bhatt AI, et al. A Comparative Testing Study of Commercial 18650-Format Lithium-Ion Battery Cells. *J Electrochem Soc.* 2015;162(8):A1592-A1600. doi:10.1149/2.0721508jes
8. Ouyang M, Zhang M, Feng X, et al. Internal short circuit detection for battery pack using equivalent parameter and consistency method. *J Power Sources.* 2015;294:272-283. doi:10.1016/j.jpowsour.2015.06.087
9. Chen M, He Y, De Zhou C, Richard Y, Wang J. Experimental Study on the Combustion Characteristics of Primary Lithium Batteries Fire. *Fire Technol.* Published online 2016. doi:10.1007/s10694-014-0450-1
10. Wang B, Ji C, Wang S, Pan S. A Detailed Finite Element Model of Internal Short Circuit and Venting During Thermal Runaway in a 32650 Lithium-Ion Battery. *Fire Technol.* 2020;56(6):2525-2544. doi:10.1007/s10694-020-00978-y
11. Shuai W, Li E, Wang H, Li Y. Space mapping-assisted optimization of a thin-walled honeycomb structure for battery packaging. *Struct Multidiscip Optim.* 2020;62(2):937-955. doi:10.1007/s00158-020-02509-3
12. Abada S, Marlair G, Lecocq A, Petit M, Sauvante-Moynot V, Huet F. Safety focused modeling of lithium-ion batteries: A review. *J Power Sources.* 2016;306:178-192.

doi:10.1016/j.jpowsour.2015.11.100

13. Soudbakhsh D, Gilaki M, Lynch W, Zhang P, Choi T, Sahraei E. Electrical response of mechanically damaged lithium-ion batteries. *Energies*. 2020;13(17):1-15. doi:10.3390/en13174284
14. Sahraei E, Campbell J, Wierzbicki T. Modeling and short circuit detection of 18650 Li-ion cells under mechanical abuse conditions. *J Power Sources*. 2012;220:360-372. doi:10.1016/j.jpowsour.2012.07.057
15. Sahraei E, Hill R, Wierzbicki T. Calibration and finite element simulation of pouch lithium-ion batteries for mechanical integrity. *J Power Sources*. 2012;201:307-321. doi:10.1016/j.jpowsour.2011.10.094
16. Bulla M, Kolling S, Sahraei E. A material model for the orthotropic and viscous behavior of separators in lithium-ion batteries under high mechanical loads. *Energies*. 2021;14(15). doi:10.3390/en14154585
17. Voyiadjis GZ, Akbari E, Kattan PI. Damage model for lithium-ion batteries with experiments and simulations. *J Energy Storage*. 2023;57(September 2022):106285. doi:10.1016/j.est.2022.106285
18. Greve L, Fehrenbach C. Mechanical testing and macro-mechanical finite element simulation of the deformation, fracture, and short circuit initiation of cylindrical Lithium ion battery cells. *J Power Sources*. 2012;214:377-385. doi:10.1016/j.jpowsour.2012.04.055
19. Ali MY, Lai WJ, Pan J. Computational models for simulations of lithium-ion battery cells under constrained compression tests. *J Power Sources*. 2013;242:325-340. doi:10.1016/j.jpowsour.2013.05.022
20. An Y, Jiang H. A finite element simulation on transient large deformation and mass diffusion in electrodes for lithium ion batteries. *Model Simul Mater Sci Eng*. 2013;21(7). doi:10.1088/0965-0393/21/7/074007
21. Wierzbicki T, Sahraei E. Homogenized mechanical properties for the jellyroll of cylindrical Lithium-ion cells. *J Power Sources*. 2013;241:467-476. doi:10.1016/j.jpowsour.2013.04.135
22. Liu B, Yin S, Xu J. Integrated computation model of lithium-ion battery subject to nail penetration. *Appl Energy*. 2016;183:278-289. doi:10.1016/j.apenergy.2016.08.101
23. Xia Y, Chen G, Zhou Q, Shi X, Shi F. Failure behaviours of 100% SOC lithium-ion battery modules under different impact loading conditions. *Eng Fail Anal*. 2017;82:149-160. doi:10.1016/j.engfailanal.2017.09.003
24. Deng J, Bae C, Marcicki J, Masias A, Miller T. Safety modelling and testing of

- lithium-ion batteries in electrified vehicles. *Nat Energy*. 2018;3(4):261-266. doi:10.1038/s41560-018-0122-3
25. Keshavarzi MM, Gilaki M, Sahraei E. Characterization of in-situ material properties of pouch lithium-ion batteries in tension from three-point bending tests. *Int J Mech Sci*. 2022;219:107090. doi:10.1016/j.ijmecsci.2022.107090
 26. Sheikh M, Rehman S, Elkady M. Numerical simulation model for short circuit prediction under compression and bending of 18650 cylindrical lithium-ion battery. *Energy Procedia*. 2018;151:187-193. doi:10.1016/j.egypro.2018.09.046
 27. Chung SH, Tancogne-Dejean T, Zhu J, Luo H, Wierzbicki T. Failure in lithium-ion batteries under transverse indentation loading. *J Power Sources*. 2018;389(September 2017):148-159. doi:10.1016/j.jpowsour.2018.04.003
 28. Bulla M, Kolling S, Sahraei E. An experimental and computational study on the orthotropic failure of separators for lithium-ion batteries. *Energies*. 2020;13(17). doi:10.3390/en13174399
 29. Yuan C, Wang L, Yin S, Xu J. Generalized separator failure criteria for internal short circuit of lithium-ion battery. *J Power Sources*. 2020;467(May):228360. doi:10.1016/j.jpowsour.2020.228360
 30. Kalnaus S, Wang Y, Turner JA. Mechanical behavior and failure mechanisms of Li-ion battery separators. *J Power Sources*. 2017;348:255-263. doi:10.1016/j.jpowsour.2017.03.003
 31. Xia Y, Wierzbicki T, Sahraei E, Zhang X. Damage of cells and battery packs due to ground impact. *J Power Sources*. 2014;267:78-97. doi:10.1016/j.jpowsour.2014.05.078
 32. Shinde SR, Song Y, Sahraei E. Modeling Electric Vehicle 's Battery Module using Computational Homogenization Approach. 2023;2023.
 33. Xu J, Liu B, Hu D. State of Charge Dependent Mechanical Integrity Behavior of 18650 Lithium-ion Batteries. *Sci Rep*. 2016;6(February):1-11. doi:10.1038/srep21829
 34. Shi F, Song Z, Ross PN, Somorjai GA, Ritchie RO, Komvopoulos K. Failure mechanisms of single-crystal silicon electrodes in lithium-ion batteries. *Nat Commun*. 2016;7(July):1-8. doi:10.1038/ncomms11886
 35. Luo H, Xia Y, Zhou Q. Mechanical damage in a lithium-ion pouch cell under indentation loads. *J Power Sources*. 2017;357:61-70. doi:10.1016/j.jpowsour.2017.04.101
 36. Zhang X, Zhu J, Sahraei E. Degradation of battery separators under charge-discharge cycles. *RSC Adv*. 2017;7(88):56099-56107. doi:10.1039/c7ra11585g

37. Luo H, Zhu J, Sahraei E, Xia Y. Adhesion strength of the cathode in lithium-ion batteries under combined tension/shear loadings. *RSC Adv.* 2018;8(8):3996-4005. doi:10.1039/c7ra12382e
38. Kalnaus S, Kumar A, Wang Y, et al. Strain distribution and failure mode of polymer separators for Li-ion batteries under biaxial loading. *J Power Sources.* 2018;378(November 2017):139-145. doi:10.1016/j.jpowsour.2017.12.029
39. Lian J, Wierzbicki T, Zhu J, Li W. Prediction of shear crack formation of lithium-ion batteries under rod indentation: Comparison of seven failure criteria. *Eng Fract Mech.* 2019;217(June):106520. doi:10.1016/j.engfracmech.2019.106520
40. Orowan E. Fracture and strength of solids. *Reports Prog Phys.* 1949;12(1):185-232. doi:10.1088/0034-4885/12/1/309
41. Wierzbicki T, Bao Y, Lee YW, Bai Y. Calibration and evaluation of seven fracture models. *Int J Mech Sci.* 2005;47(4-5):719-743. doi:10.1016/J.IJMECSCI.2005.03.003
42. Sahraei E, Hill R, Wierzbicki T. Calibration and finite element simulation of pouch lithium-ion batteries for mechanical integrity. *J Power Sources.* 2012;201:307-321. doi:10.1016/j.jpowsour.2011.10.094
43. Song Y, Gilaki M, Keshavarzi MM, Sahraei E. A universal anisotropic model for a lithium-ion cylindrical cell validated under axial, lateral, and bending loads. *Energy Sci Eng.* 2022;10(4):1431-1448. doi:10.1002/ese3.1111
44. Zhang X, Wierzbicki T. Characterization of plasticity and fracture of shell casing of lithium-ion cylindrical battery. *J Power Sources.* 2015;280:47-56. doi:10.1016/j.jpowsour.2015.01.077
45. Wang L, Yin S, Xu J. A detailed computational model for cylindrical lithium-ion batteries under mechanical loading: From cell deformation to short-circuit onset. *J Power Sources.* 2019;413(October 2018):284-292. doi:10.1016/j.jpowsour.2018.12.059
46. Gilaki M. Homogenized characterization of cylindrical Li-ion battery cells using elliptical approximation. 2021;(November):1-16. doi:10.1002/er.7531
47. Sahraei E, Meier J, Wierzbicki T. Characterizing and modeling mechanical properties and onset of short circuit for three types of lithium-ion pouch cells. *J Power Sources.* 2014;247:503-516. doi:10.1016/j.jpowsour.2013.08.056
48. Sahraei E, Kahn M, Meier J, Wierzbicki T. Modelling of cracks developed in lithium-ion cells under mechanical loading. *RSC Adv.* 2015;5(98):80369-80380. doi:10.1039/c5ra17865g
49. Zhang C, Xu J, Cao L, Wu Z, Santhanagopalan S. Constitutive behavior and

- progressive mechanical failure of electrodes in lithium-ion batteries. *J Power Sources*. 2017;357:126-137. doi:10.1016/j.jpowsour.2017.04.103
50. Sahraei E, Bosco E, Dixon B, Lai B. Microscale failure mechanism[1] E. Sahraei, E. Bosco, B. Dixon, and B. Lai, "Microscale failure mechanisms leading to internal short circuit in Li-ion batteries under complex loading scenarios," *J. Power Sources*, vol. 319, pp. 56–65, 2016, doi: 10.1016/j. *J Power Sources*. 2016;319:56-65. doi:10.1016/j.jpowsour.2016.04.005
 51. Sahraei E, Meier J, Wierzbicki T. Characterizing and modeling mechanical properties and onset of short circuit for three types of lithium-ion pouch cells. *J Power Sources*. 2014;247:503-516. doi:10.1016/j.jpowsour.2013.08.056
 52. Zhang SS, Xu K, Jow TR. The low temperature performance of Li-ion batteries. *J Power Sources*. 2003;115(1):137-140. doi:10.1016/S0378-7753(02)00618-3
 53. Huang CK, Sakamoto JS, Wolfenstine J, Surampudi S. The Limits of Low-Temperature Performance of Li-Ion Cells. *J Electrochem Soc*. 2000;147(8):2893. doi:10.1149/1.1393622
 54. Leng F, Tan CM, Pecht M. Effect of Temperature on the Aging rate of Li Ion Battery Operating above Room Temperature. *Nat Publ Gr*. Published online 2015:1-12. doi:10.1038/srep12967
 55. Kalnaus S, Wang Y, Li J, Kumar A, Turner JA. Temperature and strain rate dependent behavior of polymer separator for Li-ion batteries. *Extrem Mech Lett*. 2018;20:73-80. doi:10.1016/j.eml.2018.01.006
 56. Lamb J, Orendorff CJ. Evaluation of mechanical abuse techniques in lithium ion batteries. *J Power Sources*. 2014;247:189-196. doi:10.1016/j.jpowsour.2013.08.066
 57. An K, Barai P, Smith K, Mukherjee PP. Probing the Thermal Implications in Mechanical Degradation of Lithium-Ion Battery Electrodes. *J Electrochem Soc*. 2014;161(6):A1058-A1070. doi:10.1149/2.069406jes
 58. Rodrigues MTF, Babu G, Gullapalli H, et al. A materials perspective on Li-ion batteries at extreme temperatures. *Nat Energy*. 2017;2(8). doi:10.1038/NENERGY.2017.108
 59. Sikha G, White RE, Kumaresan K, Sikha G, White RE. Scholar Commons Thermal Model for a Li-Ion Cell Thermal Model for a Li-Ion Cell. 2008;155. doi:10.1149/1.2817888
 60. Amatucci GG, Schmutz CN, Blyr A, et al. Materials' effects on the elevated and room temperature performance of C/LiMn₂O₄ Li-ion batteries. *J Power Sources*. 1997;69(1-2):11-25. doi:10.1016/S0378-7753(97)02542-1
 61. Gilaki M, Sahraei E. Effects of temperature on mechanical response of lithium ion

- batteries to external abusive loads. In: *SAE Technical Papers*. Vol 2019-April. ; 2019. doi:10.4271/2019-01-1002
62. LePage WS, Chen Y, Kazyak E, et al. Lithium Mechanics: Roles of Strain Rate and Temperature and Implications for Lithium Metal Batteries. *J Electrochem Soc*. 2019;166(2):A89-A97. doi:10.1149/2.0221902jes
 63. Xu J, Liu B, Wang X, Hu D. Computational model of 18650 lithium-ion battery with coupled strain rate and SOC dependencies. *Appl Energy*. 2016;172:180-189. doi:10.1016/j.apenergy.2016.03.108
 64. Bulla M, Schmandt C, Kolling S, Kisters T, Sahraei E. An Experimental and Numerical Study on Charged 21700 Lithium-Ion Battery Cells under Dynamic and High Mechanical Loads. *Energies*. 2023;16(1). doi:10.3390/en16010211
 65. Xu J, Jia Y, Liu B, et al. Coupling Effect of State-of-Health and State-of-Charge on the Mechanical Integrity of Lithium-Ion Batteries. *Exp Mech*. 2018;58(4):633-643. doi:10.1007/s11340-018-0380-9
 66. Wang L, Yin S, Zhang C, Huan Y, Xu J. Mechanical characterization and modeling for anodes and cathodes in lithium-ion batteries. *J Power Sources*. 2018;392(May):265-273. doi:10.1016/j.jpowsour.2018.05.007
 67. Liu B, Jia Y, Yuan C, et al. Safety issues and mechanisms of lithium-ion battery cell upon mechanical abusive loading: A review. *Energy Storage Mater*. 2020;24(July):85-112. doi:10.1016/j.ensm.2019.06.036
 68. Reniers JM, Mulder G, Howey DA. Review and Performance Comparison of Mechanical-Chemical Degradation Models for Lithium-Ion Batteries. *J Electrochem Soc*. 2019;166(14):A3189-A3200. doi:10.1149/2.0281914jes
 69. Lu L, Han X, Li J, Hua J, Ouyang M. A review on the key issues for lithium-ion battery management in electric vehicles. *J Power Sources*. 2013;226:272-288. doi:10.1016/j.jpowsour.2012.10.060
 70. Cannarella J, Arnold CB. State of health and charge measurements in lithium-ion batteries using mechanical stress. *J Power Sources*. 2014;269:7-14. doi:10.1016/j.jpowsour.2014.07.003
 71. Li W, Xia Y, Zhu J, Luo H. State-of-Charge Dependence of Mechanical Response of Lithium-Ion Batteries: A Result of Internal Stress. *J Electrochem Soc*. 2018;165(7):A1537-A1546. doi:10.1149/2.0051809jes
 72. Wenwei W, Yiding L, Cheng L, Yuefeng S, Sheng Y. State of charge-dependent failure prediction model for cylindrical lithium-ion batteries under mechanical abuse. *Appl Energy*. 2019;251(May):113365. doi:10.1016/j.apenergy.2019.113365
 73. Iqbal N, Haq IU, Lee S. Chemo-mechanical model predicted critical SOC's for the

- mechanical stability of electrode materials in lithium-ion batteries. *Int J Mech Sci.* 2022;216. doi:10.1016/j.ijmecsci.2021.107034
74. Jia Y, Yin S, Liu B, et al. Unlocking the coupling mechanical-electrochemical behavior of lithium-ion battery upon dynamic mechanical loading. *Energy.* 2019;166:951-960. doi:10.1016/j.energy.2018.10.142
 75. Wang L, Duan X, Liu B, Li QM, Yin S, Xu J. Deformation and failure behaviors of anode in lithium-ion batteries: Model and mechanism. *J Power Sources.* 2020;448(October 2019). doi:10.1016/j.jpowsour.2019.227468
 76. Chen X, Wang T, Zhang Y, Ji H, Ji Y, Yuan Q. Dynamic mechanical behavior of prismatic lithium-ion battery upon impact. *Int J Energy Res.* 2019;43(13):7421-7432. doi:10.1002/er.4774
 77. Ying P, Wang C, Xia Y. Role of the temperature and aging in mechanical modeling of the active coating in Li-ion battery. *eTransportation.* 2023;18(August):100273. doi:10.1016/j.etrans.2023.100273
 78. Wu Z, Cao L, Hartig J, Santhanagopalan S. (Invited) Effect of Aging on Mechanical Properties of Lithium Ion Cell Components. *ECS Trans.* 2017;77(11):199-208. doi:10.1149/07711.0199ecst
 79. Ramdon S, Bhushan B. Nanomechanical characterization and mechanical integrity of unaged and aged Li-ion battery cathodes. *J Power Sources.* 2014;246:219-224. doi:10.1016/j.jpowsour.2013.07.078
 80. Waldmann T, Gorse S, Samtleben T, Schneider G, Knoblauch V, Wohlfahrt-Mehrens M. A Mechanical Aging Mechanism in Lithium-Ion Batteries. *J Electrochem Soc.* 2014;161(10):A1742-A1747. doi:10.1149/2.1001410jes
 81. Gelam SD, Maddipatla S, Chicone C, Pecht M. Core collapse in cylindrical Li-ion batteries. *J Power Sources.* 2024;623. doi:10.1016/j.jpowsour.2024.235471
 82. Carter R, Klein EJ, Atkinson RW, Love CT. Mechanical collapse as primary degradation mode in mandrel-free 18650 Li-ion cells operated at 0 °C. *J Power Sources.* 2019;437. doi:10.1016/j.jpowsour.2019.226820
 83. Müller V, Scurtu RG, Richter K, et al. Effects of Mechanical Compression on the Aging and the Expansion Behavior of Si/C-Composite|NMC811 in Different Lithium-Ion Battery Cell Formats. *J Electrochem Soc.* 2019;166(15):A3796-A3805. doi:10.1149/2.1121915jes
 84. Kouznetsova V, Brekelmans WAM, Baaijens FPT. Approach to micro-macro modeling of heterogeneous materials. *Comput Mech.* 2001;27(1):37-48. doi:10.1007/s004660000212
 85. Suquet PM. *Local and Global Aspects in the Mathematical Theory of Plasticity.*;

- 1985.
86. Galvanetto U, Aliabadi MHF. Multiscale modeling in solid mechanics: Computational approaches. *Multiscale Model Solid Mech Comput Approaches*. Published online 2009:1-334. doi:10.1142/p604
 87. Kermani G, Keshavarzi MM, Sahraei E. Deformation of lithium-ion batteries under axial loading: Analytical model and Representative Volume Element. *Energy Reports*. 2021;7:2849-2861. doi:10.1016/j.egyr.2021.05.015
 88. Kim SH, Kim SH, Huh H. Tool design in a multi-stage drawing and ironing process of a rectangular cup with a large aspect ratio using finite element analysis. *Int J Mach Tools Manuf*. Published online 2002. doi:10.1016/S0890-6955(02)00003-2
 89. Bai Y, Wierzbicki T. A new model of metal plasticity and fracture with pressure and Lode dependence. *Int J Plast*. 2008;24(6):1071-1096. doi:10.1016/j.ijplas.2007.09.004
 90. Dunand M, Mohr D. On the predictive capabilities of the shear modified Gurson and the modified Mohr-Coulomb fracture models over a wide range of stress triaxialities and Lode angles. *J Mech Phys Solids*. 2011;59(7):1374-1394. doi:10.1016/j.jmps.2011.04.006
 91. Dunand M, Mohr D. Effect of Lode parameter on plastic flow localization after proportional loading at low stress triaxialities. *J Mech Phys Solids*. 2014;66(1):133-153. doi:10.1016/j.jmps.2014.01.008
 92. Li Y, Wierzbicki T, Sutton MA, Yan J, Deng X. Mixed mode stable tearing of thin sheet AI 6061-T6 specimens: Experimental measurements and finite element simulations using a modified Mohr-Coulomb fracture criterion. *Int J Fract*. 2011;168(1):53-71. doi:10.1007/s10704-010-9554-x
 93. Clausen J, Damkilde L. A simple and efficient FEM-implementation of the Modified Mohr-Coulomb criterion. Published online 2006:0-5.
 94. Luo M, Dunand M, Mohr D. Experiments and modeling of anisotropic aluminum extrusions under multi-axial loading - Part II: Ductile fracture. *Int J Plast*. 2012;32-33:36-58. doi:10.1016/j.ijplas.2011.11.001
 95. Kermani G, Dixon B, Sahraei E. Elliptical lithium-ion batteries: Transverse and axial loadings under wet/dry conditions. *Energy Sci Eng*. 2019;7(3):890-898. doi:10.1002/ese3.318
 96. Song Y, Bulla M, Patanwala H, Sahraei E. Validation of Sahraei Failure Criterion on cylindrical and pouch Lithium-ion battery cells. *J Energy Storage*. 2024;94(April):112371. doi:10.1016/j.est.2024.112371
 97. Heugel P, Märkle W, Deich T, von Kessel O, Tübke J. Thickness change and jelly

roll deformation and its impact on the aging and lifetime of commercial 18650 cylindrical Li-ion cells with silicon containing anodes and nickel-rich cathodes. *J Energy Storage*. 2022;53(February):105101. doi:10.1016/j.est.2022.105101

98. Gilaki M, Sahraei E. Modeling state-of-charge dependent mechanical response of lithium-ion batteries with volume expansion. *Energy Reports*. 2024;12(August):3607-3619. doi:10.1016/j.egy.2024.09.041
99. Song Y, Bulla M, Patanwala H, Sahraei E. Validation of Sahraei Failure Criterion on cylindrical and pouch Lithium-ion battery cells. *J Energy Storage*. 2024;94. doi:10.1016/j.est.2024.112371
100. Kermani G, Sahraei E. Dynamic impact response of lithium-ion batteries, constitutive properties and failure model. *RSC Adv*. 2019;9(5):2464-2473. doi:10.1039/c8ra08898e
101. No Title. www.openradioss.org
102. Xu J, Liu B, Wang L, Shang S. Dynamic mechanical integrity of cylindrical lithium-ion battery cell upon crushing. *Eng Fail Anal*. 2015;53:97-110. doi:10.1016/j.engfailanal.2015.03.025
103. Zhang C, Santhanagopalan S, Sprague MA, Pesaran AA. Coupled mechanical-electrical-thermal modeling for short-circuit prediction in a lithium-ion cell under mechanical abuse. *J Power Sources*. 2015;290:102-113. doi:10.1016/j.jpowsour.2015.04.162
104. Zhang C, Xu J, Cao L, Wu Z, Santhanagopalan S. Constitutive behavior and progressive mechanical failure of electrodes in lithium-ion batteries. *J Power Sources*. 2017;357:126-137. doi:10.1016/j.jpowsour.2017.04.103

APPENDIX

1. Slope

This document is aimed to help future work to modify the Sahraei failure model in RADIOSS user material.

2. Tool

OPENRADIOSS

Install OPENRADIOSS using the following materials:

<https://github.com/OpenRadioss/OpenRadioss>

https://www.youtube.com/watch?v=Js_i7CnZty0

https://www.youtube.com/watch?v=Uo5miT_a-YY&t=841s

3. Introduction

Sahraei failure model defined the in-plane tension tensile failure strain as a function of strain ratio, in honeycomb material, let assume ε_{11} is the out of plane strain component, and ε_{22} , ε_{33} is the in-plane component.

$$c_i = \frac{\varepsilon_{compressive}}{\varepsilon_{tensile}} = \frac{\varepsilon_{33}}{\varepsilon_{11}} \text{ or } \frac{\varepsilon_{22}}{\varepsilon_{11}}$$

Where c_i is the strain ratio. This is the base governing equation of Sahraei failure model.

When considering the temperature, state of charge, strain rate and aging effects, the governing equation changes into more complex way:








$$\bullet \quad \varepsilon_f(c, T, n, SoC, \dot{\varepsilon}, cycle) = \varepsilon(c) * \left(1 - \left(\frac{T - T_r}{T_m - T_r}\right)^n\right) * (1 - c_{SoC} * SoC) * \left(1 - c_\varepsilon \ln \frac{\dot{\varepsilon}}{\dot{\varepsilon}_{st}}\right) * (1 - c_{cycle} * cycle)$$

This model is available now in EVSL backup folder:

https://tuprd.sharepoint.com/:f:/r/sites/EVSLBackUP/Shared%20Documents/Yihan%20Song/RADIOSS_model/RADIOSS_Sahraei_failure_code/sahraei_failure_0712_aging?csf=1&web=1&e=rwIbol

4. File introduction

In the folder, there are different files, the lecr04.f and f04law.f are the starter and engine file; the build_userlib Windows Batch File is the batch file you need to be able to compile the engine and starter file; the libraduser_win64.dll is the new extension library you compiled, you need copy the .dll file to the same path with your model(0000.rad and 0001.rad), then you will be able to run simulations with your new user defined material.

 build_userlib	3/25/2025 11:19 AM	Windows Batch File	5 KB
 build_userlib_win64_gfortran_7.2	4/2/2022 8:44 PM	Windows Batch File	4 KB
 f04law	8/21/2025 12:16 AM	F File	11 KB
 lecr04	7/14/2025 8:05 PM	F File	8 KB
 libraduser_win64.dll	8/21/2025 12:17 AM	Application extens...	1,402 KB
 libraduser_win64.exp	8/21/2025 12:17 AM	Exports Library File	11 KB
 libraduser_win64.lib	4/25/2025 10:07 AM	Object File Library	20 KB

5. Coding for starter file (lecr04.f)

The starter file connected the input file and the engine file, it read from the input files with all user parameter defined by the user, and assign the user parameter to the engine file.

Take user parameter **SOC** as an example:

In the starter file, we need first claim the format of the parameter **SOC**. As can be found in line 33, the **SOC** has been defined as DOUBLE PRECISION.

```

29 C-----
30      INTEGER TABLE_ID1, TABLE_ID2, TABLE_ID3, TABLE_ID4, TABLE_ID5, PTHI
31      .      ZAE1, NAE1, FAIL_ORI, COMP_DIR
32      DOUBLE PRECISION PLAMAX, VALUEX, VALUEY, EMA, ZERO, ONE, RATIO, EM05,
33      .      VOL_STRAIN, MAX_PRESSURE, SOC, TEMP, TEMP_ROOM, TEMP_MELT, T
34      STRAIN RATE STRAIN RATE COE c n c e

```

The next step is to give initial value of the parameter, sometimes if you don't initialize the value of the parameter, you will have computational errors. In line 75, the **SOC** has been given value 0 as its initial value.

```

66 C=====
67     ZERO      = 0.
68     ONE       = 1.
69     EM05      = 1.0e-5
70     TABLE_ID1 = 0
71     TABLE_ID2 = 0
72     TABLE_ID3 = 0
73     TABLE_ID4 = 0
74     TABLE_ID5 = 0
75     SOC       = 0
76     PLAMAX    = 0
77
78     NFUNC     = 0
79
80     IFUNC(1)  = 0
81     IFUNC(2)  = 0
82     IFUNC(3)  = 0
83     IFUNC(4)  = 0
84     IFUNC(5)  = 0
85     TEMP      = 0
86     TEMP_ROOM = 0
87     TEMP_MELT = 1
88     TEMP_POWER = 1
89     SOC_COE   = 0
90     STRAIN_RATE = 1
91     STRAIN_RATE_COE = 0
92     c_n       = 0
93     c_e       = 0

```

The next step is to read parameter values from the model input, here **SOC** is read from card#2, column 0 to 20 as a DOUBLE PRECISION, can be found in line 99.

```

97 c! CARD #2
98
99     READ(IIN,'(4F20.0)') SOC,SOC_COE,STRAIN_RATE,STRAIN_RATE_COE
100    IF (EMA == 0.0)   EMA = 1.0      ! no filtering
101    IF (RATIO == ZERO) RATIO = ONE
102    IF (PLAMAX == 0.0) PLAMAX= 1000.0

```

Then put the **SOC** as user parameter (UPARAM) (5)

```

145 C!          UPARAM(1) = PLAMAX
146          UPARAM(1) = TEMP
147          UPARAM(2) = TEMP_ROOM
148          UPARAM(3) = TEMP_MELT
149          UPARAM(4) = TEMP_POWER
150          UPARAM(5) = SOC
151          UPARAM(6) = SOC_COE
152          UPARAM(7) = STRAIN_RATE
153          UPARAM(8) = STRAIN_RATE_COE
154          UPARAM(9) = c_n
155          UPARAM(10) = c_e

```

One last step is writing the *SOC* in the end

```

183          WRITE(IOUT, 1500) SOC
184          WRITE(IOUT, 1600) TABLE_ID1, TEMP, TEMP_ROOM, TEMP_MELT, TEMP_
185          WRITE(IOUT, 1700) c_n, c_e
186 1000 FORMAT (
187      & 5X, '-----', //
188      & 5X, ' USER FAILURE PARAMETER', //
189      & 5X, ' created 03.04.2025 by Marian & Yihan', //
190      & 5X, ' for next Battery failure investigation.', //
191      & 5X, '-----', //)
192 1100 FORMAT (
193      & 5X, ' FUNCTION ID 1..... =', I10/,
194      & 5X, ' FUNCTION ID 2..... =', I10/)
195 1200 FORMAT (
196      & 5X, ' STRAIN_RATE..... =', E12.4/)
197 1300 FORMAT (
198      & 5X, ' STRAIN_RATE_COE..... =', E12.4/)
199 1400 FORMAT (
200      & 5X, ' SOC_COE ..... =', E12.4/)
201 1500 FORMAT (
202      & 5X, ' SOC ..... =', E12.4/)

```

6. Coding for engine file (f04law.f)

The engine file defined the failure model following the governing equation. Here, still takes **SOC** as example.

Define **SOC** as DOUBLE PRECISION (line 93)

```

83 C-----
84     INTEGER I,J,LENG,NINDX,INDX(NEL),INDX1(NEL),NCYC,ELNUM,ZAE1,NAE1,
85     .      FAIL_ORTO,COMP_DIR,NINDX1,NINDX2,FAIL_OR,INDX2(NEL),
86     .      INDX3(NEL)
87     DOUBLE PRECISION PLAMAX,PLAMAX_2,SCAL_1,SCAL_2,SCAL_3
88     DOUBLE PRECISION I1,I2,I3,
89     .      E11,E22,E33,
90     .      E_EQ,E_EQ1,E_EQ2,
91     .      Q,R,R_INTER,PHI,c_n,c_e,
92     .      ratio,ratio_2,VOL_STRAIN_LIMIT,VOL_STRAIN,P,
93     .      TT,PTHICK,SOC,EMA,RATIO_2a
94     .      DENOMINATOR,NUMERATOR,E00,MAX_PRESSURE,UN,ZERO
95     DOUBLE PRECISION TEMP,TEMP_ROOM,TEMP_MELT,TEMP_POWER,SOC_COE,STRA
96 c!    DOUBLE PRECISION EL_LEN(NEL)
97     DOUBLE PRECISION VOL_STRAIN_LIMIT2(NEL),DAMAGE(NEL),TDELE(NEL),DF
98     CHARACTER*256 LINE
99     LOGICAL :: IST DA

```

Since we define user parameter UPARAM(5) in starter file, we need to take the UPARAM(5) to engine file.

```

141     TEMP                = UPARAM(1)
142     TEMP_ROOM           = UPARAM(2)
143     TEMP_MELT           = UPARAM(3)
144     TEMP_POWER          = UPARAM(4)
145     SOC                 = UPARAM(5)
146     SOC_COE             = UPARAM(6)
147     STRAIN_RATE         = UPARAM(7)
148     STRAIN_RATE_COE    = UPARAM(8)
149     c_n                 = UPARAM(9)
150     c_e                 = UPARAM(10)

```

Then we need to define our failure strain based on governing equation. First E11/E22/E33 were assigned to EPSXX/YY/ZZ. Then calculate the strain ratio, line 225-229.

Next calculate the tensile failure strain, first, find the failure strain value based on the input curve; and calculate the final value (PLAMAX_2) based on the governing equation.

```

230 PLAMAX =FINTER(IFUNC(1),ratio,NPF,TF,DYDX)
231 PLAMAX_2=PLAMAX * (1-((TEMP-TEMP_ROOM)/(TEMP_MELT-TEMP_ROOM))**TEMP_POWER)
232 * (1-SOC*SOC COE) * (1 -STRAIN RATE COE * TT)*(1 - c n * c e)

```

Then we make a IF, if the strain value of the element is higher than PLAMAX_2, then failure happens.

```

237 IF(E33 .GE.PLAMAX_2) THEN
238   OFF(I)=0.0
239   print *, '*** element fail based on SAHRAEI1 model# ',NGL(I),' and UVAR(I,2) ', UV?
240   WRITE(LINE,'(A,I10,A,E12.4,A,E12.4,A,E12.4,A,E12.4,A,E12.4)') '*** F1 rupture el
241     " PLAMAX 2 = ",PLAMAX_2," with E11 = ",E11," with E22 = ",E22,"with E33 =
242     writing output data to the output files.
243     LENG = LEN TRIM(LINE)
244     CALL WRITE_IOUT(LINE,LENG)

```

7. Compiling the extension library.

Use Intel OneAPI , go to the working dir.

```
C:\work\user_mat\2025_08_20_mod>cd C:\work\user_mat\sahraei_failure_0712_aging
```

Then use the command to compile.

```
C:\work\user_mat\sahraei_failure_0712_aging>build_userlib.bat /STARTER "lecr04.f" /ENGINE "f04law.f"
```

Compiled completed.

```

C:\work\user_mat\sahraei_failure_0712_aging>echo off

*****
** Generating Radioss Dynamic User Library **
**      Win64 oneapi      **
*****

Preparing Library

Compiling: lecr04.f

lecr04.f

Compiling: f04law.f

f04law.f








Creating library: libraduser_win64.dll

Creating library libraduser_win64.lib and object libraduser_win64.exp







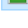
Done
-----

```

Then you will see a new .dll file

 build_userlib	3/25/2025 11:19 AM	Windows Batch File	5 KB
 build_userlib_win64_gfortran_7.2	4/2/2022 8:44 PM	Windows Batch File	4 KB
 f04law	8/21/2025 12:16 AM	F File	11 KB
 lecr04	8/21/2025 2:40 PM	F File	8 KB
 <u>libraduser_win64.dll</u>	8/21/2025 2:44 PM	Application extens...	1,402 KB
 libraduser_win64.exp	8/21/2025 2:44 PM	Exports Library File	11 KB
 libraduser_win64.lib	4/25/2025 10:07 AM	Object File Library	20 KB

Copy the .dll file into the same working dir with the model.

 libraduser_win64.dll	7/14/2025 8:06 PM	Application extens...	1,404 KB
 model_2.h3d	7/17/2025 2:39 PM	H3D File	178,182 KB
 model_2_0000	7/17/2025 1:06 PM	OUT File	3,031 KB
 model_2_0000	7/17/2025 1:05 PM	RAD File	10,339 KB
 model_2_0000_0001.rst	7/17/2025 1:06 PM	RST File	98,542 KB
 model_2_0001	7/17/2025 2:39 PM	OUT File	583 KB
 model_2_0001	3/18/2025 7:54 PM	RAD File	1 KB

In model 0000.rad file, define failure as /FAIL/USER/11, note here, the number 11 is corresponded to material 11, means you want to add the failure to material 11.

In line 101-102, card 1 is defined. In line 103- 106, card 2 is defined.

```

99 /FAIL/USER/11
100 #---1---|---2---|---3---|---4---|---5---|---6---|---7---|---8---|---9---|---10---|
101 # I_shell      Temperature      TEMP_ROOM      TEMP_MELT      Temp_power
102 #      3000          10          10          1000          1
103 #          soc          soc_coe          STRAIN_RATE      STRAIN_RATE_COE
104 #          0          0.0008          1          0.0
105 #          cycle          coe_cycle
106 #          1200          0.000015
107 #---1---|---2---|---3---|---4---|---5---|---6---|---7---|---8---|---9---|---10---|

```